



Article

A Novel Apparatus for the Simulation of Powder Spreading Procedures in Powder-Bed-Based Additive Manufacturing Processes: Design, Calibration, and Case Study

Salah Eddine Brika and Vladimir Brailovski * 

Department of Mechanical Engineering, École de Technologie Supérieure, 1100 Notre-Dame Street West, Montreal, QC H3C 1K3, Canada; salah-eddine.brika.1@etsmtl.net

* Correspondence: vladimir.brailovski@etsmtl.ca; Tel.: +1-514-396-8594

Abstract: Powder-bed-based additive manufacturing processes (PBAM) are sensitive to variations in powder feedstock characteristics, and yet the link between the powder properties and process performance is still not well established, which complicates the powder selection, quality control, and process improvement processes. An accurate assessment of the powder characteristics and behavior during recoating is important and must include the flow and packing properties of the powders, which are dependent on the application conditions. To fulfill the need for suitable powder testing techniques, a novel apparatus is developed to reproduce the generic PBAM powder spreading procedure and allow the measurements of the powder bed density, surface uniformity, and spreading forces as functions of the powder characteristics and spreading conditions, including the spreading speed and the type of spreading mechanism. This equipment could be used for research and development purposes as well as for the quality control of the PBAM powder feedstock, as showcased in this paper using a gas-atomized Ti-6Al-4V powder ($D_{10} = 25.3 \mu\text{m}$, $D_{50} = 35.8 \mu\text{m}$ and $D_{90} = 46.4 \mu\text{m}$) spread using a rigid blade by varying the recoating speed from 100 to 500 mm/s and the layer thickness from 30 to 100 μm .

Keywords: additive manufacturing; powder bed; powder feedstock; testing apparatus; powder rheology; powder bed density; powder bed uniformity; spreading forces



Citation: Brika, S.E.; Brailovski, V. A Novel Apparatus for the Simulation of Powder Spreading Procedures in Powder-Bed-Based Additive Manufacturing Processes: Design, Calibration, and Case Study. *J. Manuf. Mater. Process.* **2023**, *7*, 135. <https://doi.org/10.3390/jmmp7040135>

Academic Editor: Steven Y. Liang

Received: 28 June 2023

Revised: 20 July 2023

Accepted: 25 July 2023

Published: 28 July 2023



Copyright: © 2023 by the authors. Licensee MDPI, Basel, Switzerland. This article is an open access article distributed under the terms and conditions of the Creative Commons Attribution (CC BY) license (<https://creativecommons.org/licenses/by/4.0/>).

1. Introduction

Powder-bed-based additive manufacturing processes (PBAM), such as laser and electron beam powder bed fusion (L-PBF and EB-PFB) and binder jetting (BJ), are rapidly expanding technologies that are of particular interest in the manufacturing of complex components from a large variety of powdered feedstock materials [1–4]. All PBAM processes use a comparable design principle, starting with a powder supply module in the form of a moving platform or a hopper that deliver a specific amount of powder in increments. This powder is then processed by a separate mechanism equipped with a specific tool (scraper, roller, blade, etc.), which through its horizontal translational or rotational motion transfers the supplied powder in the form of a thin uniform layer on the building platform capable of downward movement in increments corresponding to a defined layer thickness. Once the powder layer is spread, the powder particles are selectively consolidated using different techniques (melting, sintering, binding), depending on the process used. This sequence is followed by the spreading of a new powder layer over the previously consolidated one, and the process is repeated until an entire component is built. Depending on the type of PBAM system involved (commercial or experimental), different recoating sequences and mechanisms are used, creating different powder displacement and spreading dynamics, thereby impacting both the geometric (uniformity) and physical (density) characteristics of the powder bed.

The vast majority of PBAM systems use rigid spreading blades, which are available in different profiles depending on the manufacturer. In this case, the controllable spreading parameters are the spacing between the blade and the reference surface and the displacement speed. With blade-based systems, the powders are mainly subjected to shear stresses, and the compressive stresses are minimal. Other companies use rotating roller-based systems (free rolling or motorized rotation) to spread the powder. With such configurations, the roller exerts shear and compressive stresses to spread and compact the powder. The controllable variables in this case are the spacing between the roller and the reference surface, the linear displacement speed, and the velocity and direction of rotation of the roller. Generally, rotary roller-based systems generate more compact powder beds with a smoother surface profile compared to blade-based systems thanks to a larger contact area, which allows for gradual particle rearrangement [5,6]. Nevertheless, additional compressive stresses exerted by the roller on the powder bed could potentially lead to a loss of accuracy in the effective layer thickness (loss of part precision) or even damage underlying printed structures [7–10]. To minimize disturbances on the parts being manufactured, some spreading configurations use flexible silicone blades, carbon fiber brush-based systems, or rake-toothed scrapers. Flexible blades have the advantage of being less likely to jam with the protruding artifacts of preceding layers, are more tolerant of surface imperfections, and generate lower shear stresses on the structures being fabricated. Nevertheless, wear and tear, particularly of polymeric blades, can generate less uniform spreading and include contamination in the powder bed. In addition, interference between flexible blades and surface imperfections can generate temporary jamming followed by abrupt movements of the spreading tool that can cause disturbances to the spread powder bed [11–13]. Other systems feature spreading mechanisms including mobile powder supply tanks. Such configurations can be used for the bi-directional spreading of powders to enhance the process productivity. The use of such systems with cohesive powders can be problematic, since vibrations generated by the scraper movement tend to pack powder in the tank, thereby hindering its flow into the hopper [14–18].

The uniformity of the powder layer spread on the building platform can influence the quality of a printed part, since irregular and randomly distributed layer defects (potholes, bumps, etc.) can lead to inconsistent interactions between the powder and the consolidating input (laser or electron beam, binder jet) [19,20]. The powder bed density is yet another key characteristic of the powder bed, and as it increases, so does the density, the uniformity, and the precision of a printed part [21–25]. Furthermore, since the forces applied by a spreading tool during powder recoating on the previously consolidated features could jeopardize the integrity of the components being built, such forces must be minimized, especially when the components are complex and delicate (lattice- or cellular-based structures, for example). It must also be mentioned that the powder spreading (recoating) speed impacts the process productivity, since the recoating operation could take from 30 to 50% of the total building time, depending on the geometry and build orientation of the printed part and the printing parameters used [26–28]. In summary, the uniformity and density of the powder bed, as well as the forces and velocities of the recoating procedure, constitute the principal characteristics of any powder recoating process and directly influence the service properties of the printed parts and the process productivity.

The characteristics of any powder recoating system cannot be analyzed separately from those of the powder feedstock. Depending on the powder production route and material, the characteristics of the powder feedstock vary in terms of the chemical composition, particle size distribution (PSD), morphology, density, and surface properties [29,30]. A number of studies have demonstrated a significant impact of the above-mentioned characteristics on the performances of PBAM parts [29,31–39]. Selecting the most suitable powder for a given piece of manufacturing equipment can be challenging, considering the broad variety of products available, and the choice is generally guided by the manufacturers' recommendations. While following these recommendations in the context of an industrial application allows savings of money and time, in an R&D environment, evaluating the

suitability of a given powder for a specific piece of PBAM equipment, and specifically its spreadability characteristics, could form an integral part of any research workflow.

Several powder flowability characterization techniques are commercially available, namely funnel-based methods (Hall, Carney, Gustavsson), shear cells, avalanche testers, and powder rheometers, all characterizing powders under different conditions. Using the results obtained with the above-mentioned techniques to assess the feedstock spreadability in the context of a specific piece of PBAM equipment can be challenging, since this property is not an intrinsic powder characteristic but rather a powder property that is strongly dependent on the testing conditions applied. This difficulty can be mitigated by subjecting the powder to testing conditions that are as close to those of a simulated manufacturing process as possible. Unfortunately, a harsh working environment and the closed architecture of commercial PBAM equipment, in addition to costly and time-consuming printing processes, limit the possibilities of conducting in situ powder flowability characterization experiments. Because of these limitations, there is a clear need for a testing apparatus capable of characterizing powder spreadability levels under simulated application conditions. Such an apparatus must be equipped with instrumented devices enabling parametric studies of the metrics of interest, while being versatile enough to reproduce the specific spreading conditions created by different powder distribution mechanisms used in commercial PBAM equipment.

Different testing devices dedicated to powder spreadability investigations have been introduced in the literature. Table 1 summarizes the most representative studies by providing brief descriptions of the proposed apparatuses, types of spreading mechanisms involved, controlled variables, metrics of interest, measurement principles, and degrees of conformity of the proposed technical solutions with targeted commercial PBAM systems. For each apparatus, a basic rating system (low, moderate, or high) is used to define the process representativity as an indication of how accurately the proposed apparatus simulates the conditions and spreading sequences of commercial equipment. Hereafter, short descriptions of the developed testers are provided, sorted by the levels of sophistication, starting from more simplistic solutions and moving to more advanced systems, with the intent to establish the main objectives of this work.

Simplistic and straightforward methods were introduced in [40–43]. Beitz et al. [41] proposed an apparatus fitted with scrapers of different shapes, spreading one layer of powder on the detachable platform at a time. Here, the surface quality and the density of a powder bed were analyzed using the optical microscopy and computed tomography techniques. Ahmed et al. [40] proposed spreading the powder manually using a cardboard stencil with a gap corresponding to a desired layer thickness and to examine the obtained layer using scanning electron microscopy in order to evaluate the powder coverage as a function of the layer thickness and the PSD of the powders tested. In order to mimic conventional scraper- and hopper-based spreading mechanisms, Cordova et al. [42] introduced some applicator tools to manually spread one layer of powder at a time. The dimensions of a patch formed by spreading a known amount of powder were used to estimate the volume of powder spread and the approximate apparent density of the powder bed. Finally, Lefebvre et al. [43] assessed the powder spreadability using a Hegman gauge (100 μm). The method consisted of placing a small quantity of powder in a groove whose depths varied from 100 μm to ~ 0 μm and then spreading the powder (from 100 to 0 μm thickness) along the groove using a blade. In this case, the spreadability was assessed qualitatively by comparing the uniformity levels of the deposited powder layers.

More versatile and automated systems than the above-mentioned ones were proposed in [44–50]. Among them, Le et al. [44] introduced the idea of scanning a single layer of spread powder using a contact image sensor (CIS) installed behind the spreading mechanism (hopper/scrapper) to study the powder bed quality levels obtained with different spreading strategies. Hulme-Smith et al. [45] repurposed a film applicator device by adding a doctor blade to spread one layer of powder at a time and added an imaging system to evaluate the degree of surface coverage as a function of the recoating speed for powders

with different particle size distributions and chemical compositions. Lee et al. [46] measured the angle of the avalanche formed during the spreading of a single layer of powder using a camera aligned with the scraper from their testing system to compare different recoating speeds and layer thicknesses. The apparatus developed by Snow [47] used the spreading platform and the blade of a commercial system (EOS M280) coupled with a microscope, a camera, and a laser profilometer to respectively analyze the avalanche angle, the surface coverage, and the roughness of a single spread layer. Lupo et al. [50] presented a setup with a motorized spreading arm, where a blade with an adjustable inclination angle or roller recoater can be mounted to spread the powder on deposition plates with different depths to mimic different layer thicknesses. A microscope was installed to capture pictures of the powder bed to analyze the spreading uniformity. Mehrabi et al. [49] proposed a rig where the controlled movement of a spreading arm fills a pocket of 1 mm depth. The deposited powder is collected and weighted *ex situ* to evaluate the deposited powder bed density. Finally, Van den Eynde et al. [48] attached the building platform to an analytical balance to evaluate the mass of a deposited layer in order to estimate the powder bed density of feedstocks with different PSDs and particle morphologies.

Furthermore, a series of advanced and highly automated testers were presented in [17,51,52]. Oropeza et al. [17] proposed a testing system containing two motorized platforms for controlled powder supply and spreading, a modular powder spreading mechanism capable of using different spreading tools (e.g., motorized roller, stiff or flexible scraper, hopper), and an imaging system overhanging the powder bed. This testing system was designed to study the impact of a spreading mechanism and the layer thickness on the powder bed uniformity. Mitterlehner et al. [51] presented a test bench also containing two motorized platforms, one for powder supply and another for powder spreading, and a recoating mechanism with an adjustable recoater blade angle. After the recoating operation, the spreading platform can be extracted from the tester and installed on the table of an optical microscope to analyze the degree of surface coverage, the layer roughness, and the flatness of the powder bed. A similar apparatus was developed by Yee et al. [52], with the possibility of an *in situ* evaluation of the surface roughness of the powder bed using a camera attached to the apparatus. Escano et al. [53] proposed an apparatus consisting of a motorized scraper and platform adapted to be mounted in an X-ray computed tomography machine to visualize the particle dynamics during spreading, the density, and the surface profile of the formed powder bed. Lhuissier et al. [54] proposed a miniature design of the L-PBF machine including a spreading system, moving platforms, laser module, and controlled environment chamber, which is compatible for mounting in an X-ray tomograph to analyze powder spreading and consolidation dynamics.

To sum up, most of the above proposed solutions are mainly focused on evaluations of powder bed uniformity [17,40,43–45,51,52], while some apparatuses combine an assessment of the powder bed uniformity with that of the powder spreadability [46,47]. Another group of technical solutions consider the powder bed density as the main metric of interest [42] or combine the powder bed density measurements with the powder bed uniformity assessments [41,48]. To date, no reported testing system has proposed an integral solution that concurrently measures all metrics of interest relevant to powder spreading during the PBAM processes, namely the powder bed density, the powder bed uniformity, and the powder spreading forces, with a significant level of automation of the elements involved in the spreading operation. It is reasonable to assume that a testing system capable of measuring the above-mentioned metrics of interest simultaneously would allow for conducting pertinent powder experiments. However, to be a relevant characterization tool, such an apparatus must be able to reproduce the spreading conditions of commercial machines as closely as possible (i.e., controlled spreader movements and velocities, precise displacements of the platforms, and multi-layer testing). Moreover, the equipment must be versatile enough to allow the use of different types of spreading mechanisms, variable spreading velocities, displacements of the platforms, and recoating sequences. Such a testing apparatus would be a valuable control tool for the selection and quality control

of a suitable feedstock for a given PBAM process or system, as well as a relevant asset for minimizing the spreading time by optimizing the recoating speed, the movements of powder supply and spreading or building platforms, and the design of a spreading mechanism.

Table 1. Major technical specifications of the selected powder spreadability testers reported in the literature.

Degree of the Process Representativity	Spreading Mechanism	Level of Motorization	Multi-Layer Possibility	Controlled Process Variables	Measured Metrics	In-Situ Measurement Possibility	Ref.
Low	Makeshift cardboard stencil	N/A	No	Layer thickness	Surface coverage	No (SEM)	[40]
	Scraper or Funnel	N/A	No	Powder state (as-received, air-dried, vacuum-dried, moisturized)	Apparent density	No (volume estimation using a ruler)	[42]
	Scraper	N/A	No	Blade type/shape/material	Surface quality	No (LSM, XMT)	[41]
	Scraper	N/A	No	Powder state	Surface quality	No	[43]
Moderate	Hopper + scraper	Motorized spreader	No	Spreading velocity Blade type/shape/material Layer thickness	Layer thickness Surface roughness Particle density	Yes (image sensor CIS)	[44]
	Scraper	Motorized spreader	No	Spreading velocity Layer thickness	Coverage area	Yes (camera pointed at the test platform)	[45]
	Scraper	Motorized spreading platform (horizontal movements)	Yes (Manual)	Spreading velocity Layer thickness	Avalanche angle	Yes (camera aligned with the recoater blade)	[46]
	Scraper	Motorized spreader	No	Spreading velocity Scraper material Layer thickness	Avalanche angle Surface coverage Surface roughness	Yes (microscope, camera, laser profilometer)	[47]
	Scraper	Motorized spreader	Yes (Manual)	Layer thickness Spreading velocity Spreader type	Surface quality Packing density	Yes (analytical balance)	[48]
	Scraper (adjustable angle)—roller	Motorized spreader	Yes (spreading plate thickness)	Layer thickness Spreading velocity Spreader type	Layer uniformity	Yes (microscope)	[50]
	Scraper	Motorized spreader	No	Spreading velocity Scraper gap	Powder bed density	No (analytical balance)	[49]
	Motorized dispenser + Scraper Roller Hopper	Motorized spreader Motorized dispenser Motorized spreading platform	Yes (Motorized)	Number of spread layers Layers thickness Spreading velocity Type of scraper	Layer uniformity	Yes (camera and coaxial light setup)	[17]
High	Motorized dispenser + Scraper	Motorized spreader Motorized dispenser Motorized spreading platform	Yes (Motorized)	Number of spread layers Layers thickness Spreading velocity Distance between blade and building platform Angle of recoater blade	Surface coverage Surface roughness Surface flatness	No (digital microscope)	[51]
	Motorized dispenser + Scraper	Motorized spreader Motorized dispenser Motorized spreading platform	Yes (Motorized)	Spreading velocity Layer thickness	Surface roughness	Yes (camera and lightning setup)	[52]
	Motorized scraper	Motorized spreader Motorized spreading platform	No	Spreading velocity Layer thickness	Dynamic repose angle Layer uniformity	Yes (X-ray computed tomography)	[53]
	Motorized dispenser + Scraper	Motorized spreader Motorized dispenser Motorized spreading platform	Yes	Spreading velocity Layer thickness Type of scraper Number of spread layers	Layer uniformity	Yes (X-ray computed tomography)	[54]

To provide such a technical solution, this work focuses on the design and validation of a novel powder testing apparatus intended to simulate the powder spreading process in some of the most frequently used commercial powder-bed-based AM systems. The proposed solution allows a controlled multi-layer translational powder to be spread using interchangeable recoating devices. The instrumented tester allows us to measure the powder bed density, the spread layer uniformity, and the spreading forces for different recoating strategies and feedstocks. The functionality and capabilities of the main sub-assemblies of a proposed tester are described and a case study involving the testing of a specific AM powder feedstock is finally carried out to illustrate the capabilities and limitations of the apparatus developed.

2. Design and Description of the Powder Spreading Apparatus

The powder spreading apparatus is designed as a consolidated tabletop unit (467 × 294 × 678 mm) adapted for spreading different material types (polymer, ceramic, metal) in powdered form and includes all of the main elements needed to reproduce the recoating operations of most commercial PBAM systems. It is equipped with instrumentation to monitor the metrics of interest, namely the powder bed density, layer quality and uniformity, and spreading forces. The main structural elements of the apparatus in contact with the powder to be tested are made of 6061 aluminum to ensure a good balance between strength, machinability, and corrosion resistance, in addition to being paramagnetic to prevent the electro-charging of ferromagnetic powder particles.

The following are the main components of the apparatus (Figure 1): the powder dispensing module, consisting of the dispensing platform (1), the actuator (2) and the dispensing duct (3); the powder spreading module, consisting of the spreading platform (4) controlled by the actuator (5) and equipped with the load cells (6); the spreading mechanism, consisting of the spreading arm (7), the actuator (8) monitored by a torque sensor (9), and two limit switches (10); the powder bed uniformity control module, consisting of the CCD camera (11) and the 3D scanner (12). In addition to the other main components, the apparatus includes the powder collector (13), the control panel (14), and the main platform (15). The control architecture and pictures of the testing apparatus are presented in Appendix A, while a detailed description of the main components is presented in the following sections.

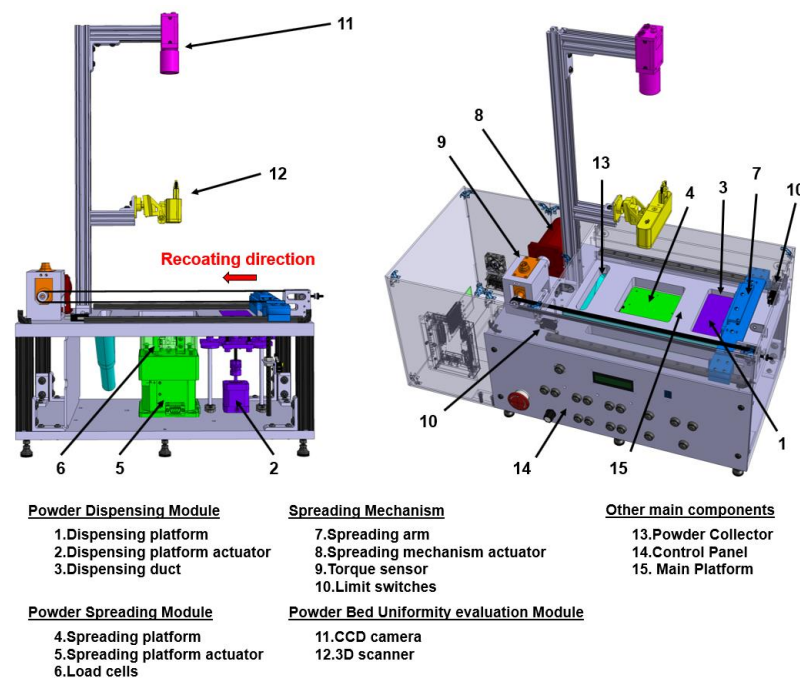


Figure 1. Design of the powder spreading apparatus with the list of the main components.

2.1. Powder Dispensing Module

The dispensing module transfers the powder required for spreading from the dispensing duct (3 in Figure 1) to the spreading platform (4 in Figure 1). A schematic of the dispensing elevator module is presented in Figure 2, along with the list of main components. The dispensing system comprises a stepper motor (Nema 17HD48002H-22B 12V stepper motor, ZYLtech, Houston, TX, USA; 1 in Figure 2) that controls vertical movements of the dispensing platform (7 in Figure 2) through the dispensing duct within a 20 mm travel distance using two guide shafts (carbon steel, 1/4" diameter; 8 in Figure 2) and a precision lead screw (0.216"-20.8 thread size; 3 in Figure 2) linked to the motor via a shaft coupling (2 in Figure 2). A silicon seal is installed in the groove (4 in Figure 2) at the base of the dispensing platform to minimize powder leakage. The stepper motor (1) is controlled via a driver (DRV8825, 2.2 A, 8.5–45 V, Texas instruments, Dallas, TX, USA) in combination with a microcontroller (ARDUINO MEGA 2560, ARDUINO, Ivrea, Italy), with the displacement increments being defined by the number of steps during the motor rotation, while the displacement speed is defined by the delay between the steps during the actuator spin. Two limit switches (V-156-1A5; OMRON, Osaka, Japan, 5 and 6 in Figure 2) are installed to define the upper and lower end positions of the platform and to stop the displacement of the motor once activated.

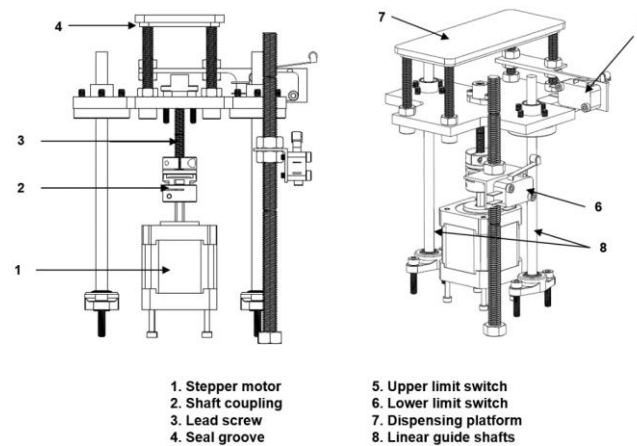


Figure 2. Schematic of the powder dispensing module.

The dispensing platform is initially placed at the lowest position and moves upwards using the operator-defined increments. The dispensing module can contain up to 120 cm³ of powder when the platform is at its lowest position. Since the dimensions of the dispensing (120 mm × 50 mm) and spreading (100 mm × 100 mm) platforms are different, the displacement increment of the dispensing platform is defined by Equation (1):

$$\text{Dispenser displacement} = \frac{\text{Spreading platform area} \times \text{Layer thickness}}{\text{Dispensing platform area}} \times \text{Charge amount}(\%) \quad (1)$$

to ensure that the amount of powder available for spreading is sufficient to entirely cover the spreading platform with a uniform layer of powder of a given thickness.

2.2. Powder Spreading Module with Weighing Unit

The spreading platform (1 in Figure 3) contains powder spread by the recoating mechanism. The platform emulates the part building area in a commercial PBAM machine. A schematic of the spreading elevator module is presented in Figure 3, along with a list of the main components. The spreading module comprises a motorized vertical stage (8MVT100-25-12V-1.8A, STANDA, Vilnius, Lithuania; 2 in Figure 3) that controls vertical movements of the platform through the corresponding duct within a 20 mm travel distance. The motorized vertical stage is capable of a reported 5 μm resolution when controlled in full-step mode.

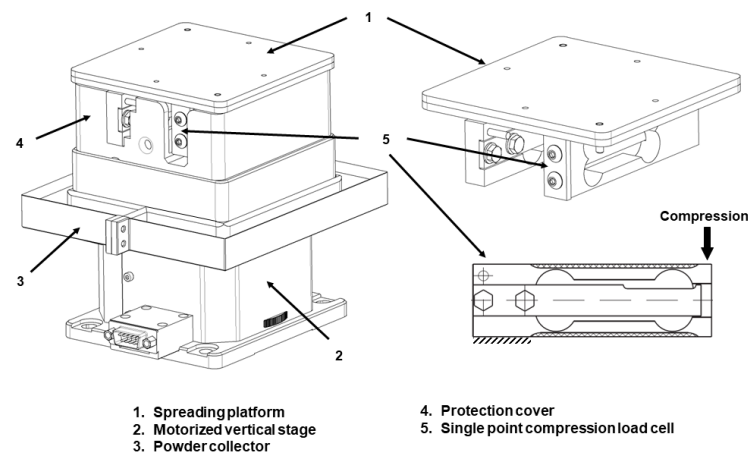


Figure 3. Schematic of the powder spreading module with the weighing unit.

The stepper motor of the vertical motorized stage is controlled using the same principle as that used to control the dispensing platform actuator (1 in Figure 2), as described in the previous section. The displacement increments of the platform, corresponding to the layer thickness of the deposited powder bed, are defined by the operator. The platform is initially placed at the same level as the main platform (15 in Figure 1), and it moves downward by defined increments. At its lowest position, the spreading platform can contain up to 200 cm³ of powder. The limit switches embedded in the motorized vertical stage unit (8MVT100-25-12V-1.8A, STANDA, Vilnius, Lithuania,) are used to define the limit positions of the platform during its displacements.

A weighing unit is included within the spreading platform module in order to measure the mass of the deposited powder. Two single point load cells (108AA aluminum single-point load cell; ANYLOAD, East Hanover, NJ, USA, 5 in Figure 3) are installed under the spreading platform and attached to the upper surface of the motorized vertical stage to form a unique mechanical link between the two platforms, such that the load generated by the deposited powder layers is fully applied on the load cells with a minimum of interference. Each load cell has a maximum rated capacity of 300 g, with a full-scale output of 1 mV/V \pm 20% and non-linearity and repeatability factors below \pm 0.023%. The load cells are attached to amplifiers (EMBSGB200, TACUNA SYSTEMS, Golden, CO, USA), including an offset adjusting potentiometer and DIP (Dual In-line Package) switches to configure the reading gain. A total gain of 1100 was selected to offer a good compromise between the reading sensitivity and stability (reduced signal noise), without saturating the readings when applying the maximum load defined around 500 g. The amplifiers are connected to the microcontroller (ARDUINO MEGA 2560, ARDUINO, Ivrea, Italy) via an analog input to convert the voltage changes (0 to 5 V) into digital readings (0 to 1024 bit). More details about the calibration and capabilities of the weighing unit are presented in Section 4.1. For each powder spread layer, 10⁴ readings from each load cell are recorded, averaged, and summed together to estimate the total load applied by a deposited amount of powder. The digital readings are converted into mass values using the formula established during the calibration phase described in Section 4.1.

The spreading platform is leveled with the main platform using an electronic level gauge and centered so as to get a consistent gap 0.1 mm gap between the contour of the platform and the inner surface of the travel duct. This gap serves to minimize the weighing unit reading disturbances and even the jamming of the spreading platform caused by powder particles filling the interstice between platforms. The gaps allow a small quantity of powder to freely fall into the powder collector (3 in Figure 3) installed underneath, which is cleaned after each testing sequence. The impact of the gap between the platforms will be discussed in Section 4.1. A cover (4 in Figure 3) is added to protect the load cells from the falling powder particles and prevent them from accumulating around the sensors.

2.3. Spreading Mechanism with Recoating Forces Measurement Unit

The spreading mechanism uses a horizontally moving recoating tool to evenly distribute and transport the powder from the dispensing platform to the spreading platform. The spreading mechanism comprises an actuator, a linearly guided moving carriage, and a spreading tool. A brushless servo motor (BLM-N23-50-1000-B, 55 oz-in, 4.6 A, GALIL MOTION CONTROL, Rocklin, CA, USA) (8 in Figure 1) associated with a belt (GT2, 6 mm, rubber with fiberglass core) and linear guide rails (12 mm wide, 27 mm wide aluminum sleeve bearing carriage) moves the spreading arm horizontally from one side of the apparatus testing area to the other. The actuator is controlled via a dedicated driver (DMC-31012-BOX MO-ISCNTL-LSNK, GALIL MOTION CONTROL, Rocklin, CA, USA). The end positions of the recoating arm are detected by two limit switches (V-156-1A5, OMRON, Osaka, Japan, 10 in Figure 1), which automatically stop the spreading arm movement once one of the end positions is reached. The motor is associated with a differential quadrature incremental encoder (1000 lines, 4000 count per revolution) allowing one to monitor and adjust the actuator velocity to match the speed specified by the operator using a PID controller. The current configuration allows one to securely and consistently displace the moving carriage within a 20 to 800 mm/s speed range.

A modular recoating module (7 in Figure 1) is developed to allow the mounting of interchangeable spreading tools on the horizontally moving carriage. Figure 4 shows the assembly of the blade and the roller spreading configurations. A set of custom blades, made from different materials (metal or polymer, stiff or compliant) and different geometries (thickness, contact angle), can be mounted on the moving cart (1 in Figure 4) via an L-shaped bracket (5 in Figure 4). The height, the tilt, and the leveling of the blade can be adjusted using a set of four screws and springs (4 and 6 in Figure 4). Rollers (11 in Figure 4) with embedded bearings (14 in Figure 4) (RORLS20-8-LC125, MISUMI, Chicago, IL, USA) made from different materials (steel, aluminum, urethane) can be fitted on the moving cart using a dedicated mounting bracket (13 in Figure 4), a set of positioning pins (10 in Figure 4) with screws, and springs for height adjustment (9 and 12 in Figure 4). The clearance between the blade or roller and the spreading platform of the apparatus is controlled using shims of known thicknesses.

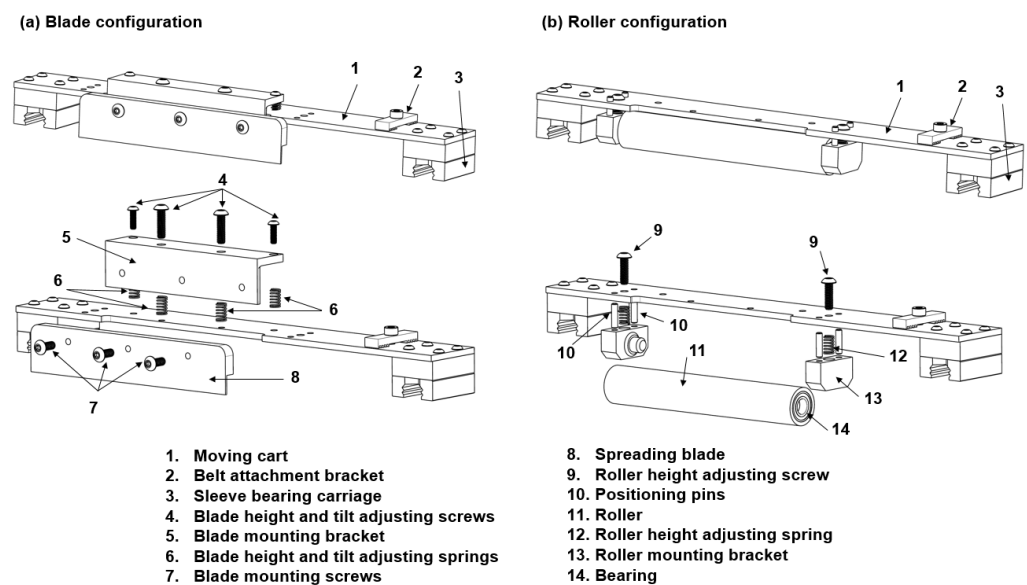


Figure 4. Assembly schematic of the powder spreading arm: (a) blade setup; (b) roller setup.

To monitor the spreading forces during the displacement of the moving carriage, a shaft-to-shaft rotary torque sensor (TRS605-FSH02054, FUTEK, Irvine, CA, USA, 9 in Figure 1) is coupled with the actuator on one extremity of the main shaft and with the drive pulley on its other extremity. The torque sensor has a maximum rated capacity of 5 N·m,

with non-linearity and repeatability factors of $\pm 0.2\%$ of the rated output. The sensor is attached to a signal conditioner module (FSH03631, FUTEK, Irvine, CA, USA) that includes a power supply unit and an analog-to-digital converter unit. The software SENSIT 2.10 provided by the sensor manufacturer is used to set the sampling rate to 1200 Hz with a 16-bit resolution and to record the data.

2.4. Powder Bed Uniformity Evaluation Module

To assess the powder bed uniformity, two independent imaging systems (optical camera and 3D scanner) are mounted on the apparatus. The optical imaging system comprises a CCD camera (GRAS-20S4M-C, 2.0 MP, 30 FPS, monochromatic, POINT GREY, Los Angeles, CA, USA) and a lens (LM35JC, KOWA, Duesseldorf, Germany), as shown respectively as 1 and 2 in Figure 5. The camera is connected to a computer via its dedicated network interface card (IEEE-1394 PCI card) and controlled via FlyCapture software 2.5 provided by the camera manufacturer. The working distance between the camera and the spreading platform (5 in Figure 5) is defined to provide a field of view of 101×101 mm (102% of the spreading platform area) and an object space resolution of $83.3 \mu\text{m}$ (smallest detectable feature).

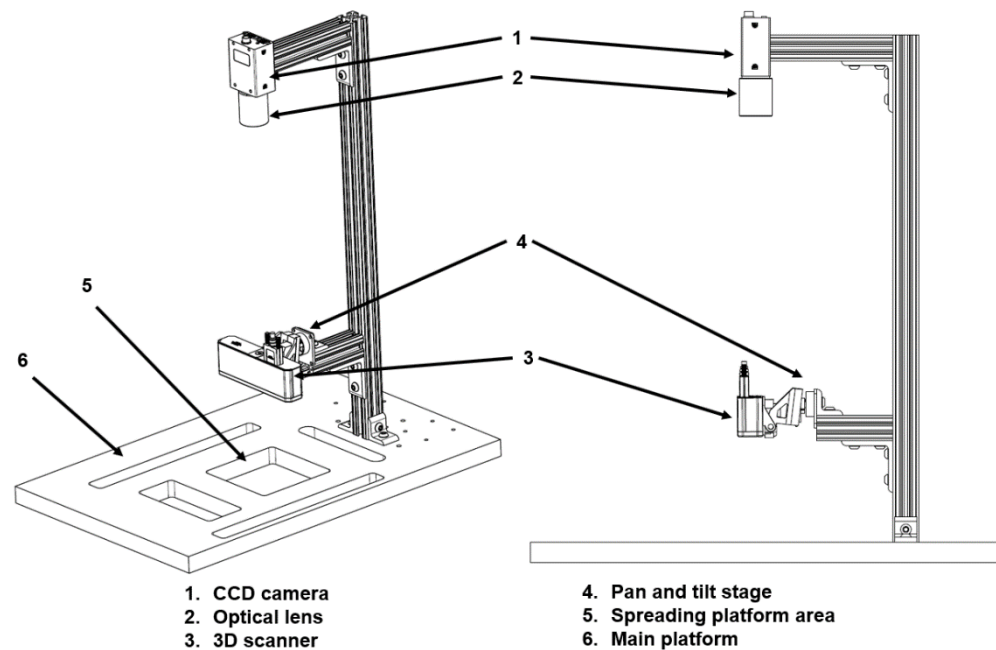


Figure 5. Schematics of the powder bed uniformity evaluation module.

A 3D scanner (REVOPOINT MINI, REVOPOINT 3D Technologies, Inc., Shenzhen, China) shown as 3 in Figure 5 is mounted on a pan and tilt stage (4 in Figure 5) above the spreading platform. The scanner employs binocular blue light technology to project structured light patterns on the powder bed. A dual camera system captures the projected patterns from different angles. The scanner software analyzes images of the reflected light pattern to determine the distance between the scanner and each point on the studied surface based on the distortions in the pattern that occur due to the object shape. The scanner is mounted on a miniature pan and tilt stage equipped with two micro-servomotors (SG90, TOWER PRO, Hunt Valley, MD, USA) and controlled by the ARDUINO MEGA 2560 microcontroller to perform a $\pm 30^\circ$ pan and tilt displacement. The scanner is connected to a computer via USB and controlled using the dedicated software REVO SCAN 5.2.1. The working distance between the scanner and the spreading platform is defined as 100 mm. The movements of the pan and tilt mounting stage covers the spreading platform and the adjacent area (~ 10 mm around the platform) under different angles to capture a total of 456 frames. The point cloud of the scanned surface is generated and saved. It should be

noted that the 3D scanner is removed from the field of view of the CCD camera when the latter must be used to capture the pictures.

3. Testing Procedure

Before starting the test, the operator prepares the apparatus by cleaning its main components using an industrial vacuum and collecting the remaining powder or dust using a soft laboratory wipe and isopropanol. After turning on the apparatus and letting it warm up for at least 20 min to stabilize the operating temperature of the electronic components, the operator defines the spreading parameters using the front control panel or by editing the program using a computer. The operator then proceeds to homing the different moving components, namely the recoating arm (right side of the apparatus), the dispensing platform (lowest vertical position), and the spreading plate (highest vertical position). The load cell reading offsets are checked and adjusted using the integrated potentiometer to ensure that both cells display identical readings when no load is applied. The operator can use calibrated weights to initialize the readings of the weighing unit. Reference readings of the torque sensor are recorded for a given spreading arm velocity with no powder present (no load, torque variations induced by the setup are recorded). The gap between the spreading tool and the main platform is checked using shims and rectified, if needed, using the set screws (4 in Figure 4). The operator then proceeds by filling the powder in the dispensing duct and levelling it with a dedicated scraper to remove any excess. Once the apparatus is prepared, the operator begins the test sequence by pressing the start button of the control panel. Figure A4 (Appendix B) presents a diagram describing the test sequence of the powder spreading apparatus.

At the beginning of a test, the temperature and humidity in the room are recorded by the embedded DHT111 sensor (ADAFRUIT, New York, NY, USA), the dispensing platform moves up, and the spreading platform is lowered by increments defined by the user. Next, the recoating arm moves from the right end position to the left end position (until the left position limit switch is activated) at the velocity defined by the operator. Simultaneously, during the spreading arm displacement, the motor torque variations are recorded to evaluate the powder spreading forces. For each spread powder layer, the mass of a deposited powder is measured using the load cells and the obtained data are saved.

The dispensing and spreading platforms are then lowered by a small increment to a safe position such that the spreading arm can move to the right end position without collision and without damaging the previously spread powder layer. Once the spreading arm is at the right end position, the dispensing and spreading platforms return to the previous positions (prior to the return of the spreading arm). This sequence is repeated until the required number of layers defined by the operator is reached, the dispensing or spreading platforms reach one of their limit end positions, or the operator decides to interrupt the test by pressing the pause or stop buttons on the front panel. At the end of the spreading sequence, using the imaging system, the operator saves a picture of the deposited powder layer via FlyCapture 2.5 software and performs an acquisition test of the powder bed topography using a 3D scanner and REVO SCAN 5.2.1 software.

4. Validation and Calibration

To ensure the validity of the measurements of the main metrics of interest, namely the powder layer density, the powder bed uniformity, and the spreading forces, the following systems were calibrated: the weighing unit, the imaging system, the dispensing and spreading platform displacement indicators, and the torque sensor of the spreading arm mechanism.

4.1. Weighing Unit

Calibrated weights ranging from 0.01 g to 400 g were used to calibrate and test the capabilities of the weighing unit. The test consists of three repetitions of a sequence and starts by placing the weights in ascending order, in descending order, and then in

randomized order. For each placed weight, 10^4 readings are recorded. Between each repetition, the system is left unloaded for at least 20 min. Following the three repetitions of the defined sequence, the results obtained for each weight are combined, the readings of the two load cells are summarized, and the average and standard deviation are calculated. Figure 6a shows the digital readings (sum of both load cells) as functions of the placed weights. It can be seen that the readings are highly linear, with an R-squared value very close to unity ($R^2 = 99.98\%$). The obtained results were used to establish the conversion equation (Equation (2)) that will allow the evaluation of the mass of the deposited powder as a function of the obtained digital readings.

$$\text{Mass of deposited powder} = 0.2409 \times \text{Digital reading} - 160.72 \quad (2)$$

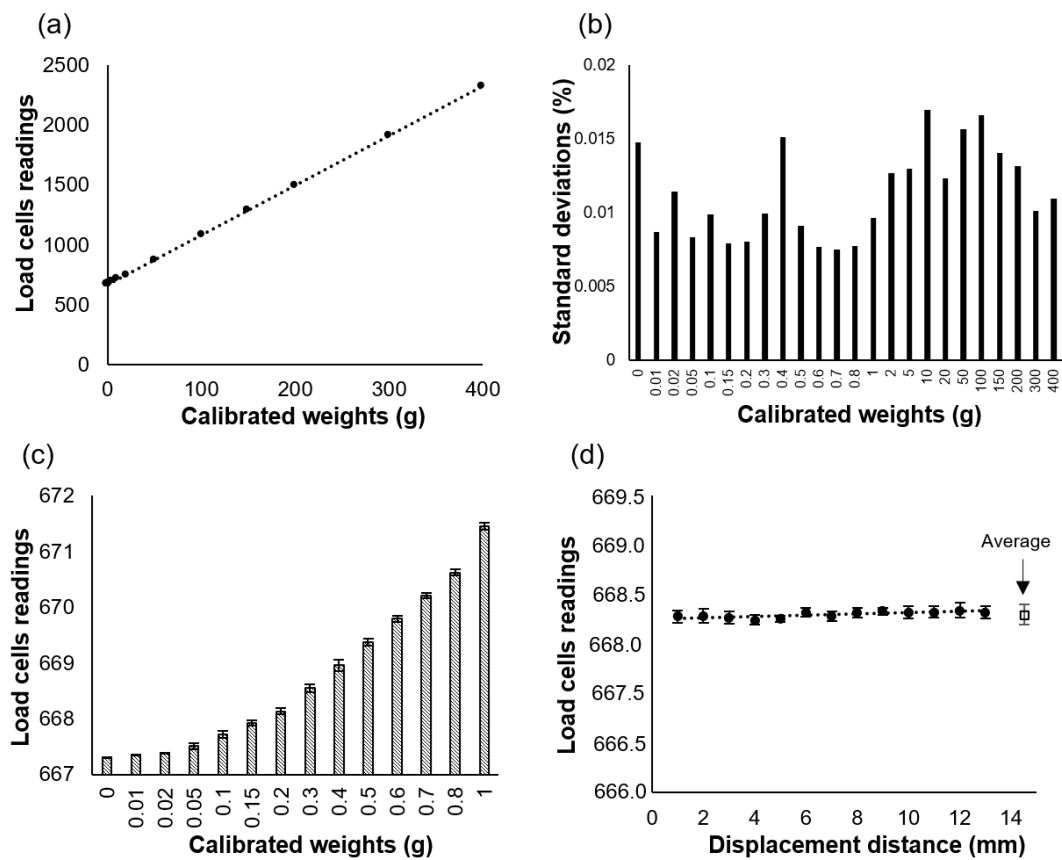


Figure 6. Weighing unit calibration and capabilities: (a) linearity; (b) variability; (c) sensitivity to small mass variations; (d) stability as a function of the travel distance.

It should be noted that prior to the start of the test sequence with the powder (Figure A4, Appendix B), the operator can recalibrate the load cells by placing different known weights and adjust the numerical factors of Equation (2) accordingly.

The standard deviation error bars are plotted in Figure 6a but cannot be seen because of the small values obtained and the good repeatability of the results, as shown in Figure 6b, where the readings' standard deviations in terms of percentage of the measured value for each calibrated weight are plotted. The average calculated standard deviation is 0.011% and the maximum is 0.017%. Figure 6c shows the sensitivity of the unit readings to small calibrated weights. The Student's test (*t*-test) allows us to conclude that the differences between the measurements are statistically significant. The smallest mass variation detectable by the weighing unit is 0.01 g (smaller calibrated weights were not available to test smaller increments). Figure 6d shows the reading stability of the load cells during the downward motion of the spreading platform (without weights or powder)

through a travel distance of 13 mm within the corresponding duct. The maximum reading variation during the platform displacement is 0.016%.

To assess the powder bed density, the mass measured by the weighing unit must be divided by the volume of the deposited powder, with the latter being calculated as a product of the platform surface area multiplied by its vertical displacement. However, as mentioned in Section 2.2, a 0.1 mm gap is left between the contours of the spreading platform and the duct of the main platform in order to minimize the disturbances of weighing unit readings caused by friction during the platform’s downward displacements. The gaps allow a small quantity of powder to fall into the collector installed underneath, inducing the creation of a powder bed with sloping edges, as shown in Figure 7. The estimated volume used to calculate the powder bed density should be adjusted accordingly. The missing powder volume caused by the sloping edges can be estimated by calculating the area of a triangle formed by the contour of the powder bed (Figure 7) multiplied by the spreading platform perimeter. The triangle base “a” is measured using the imaging system installed above the powder bed (Figure 7), while the triangle height “b” corresponds to the known platform’s vertical displacement. Thus, the adjusted volume of the deposited powder bed can be calculated using Equation (3) and the powder bed density can be estimated using Equation (4):

$$\text{Adjusted volume} = (\text{spreading platform area} \times b) - (a \times b \times \text{spreading platform perimeter} / 2) \tag{3}$$

$$\text{Powder bed density} = \frac{\text{Mass of deposited powder}_{(\text{Displacement distance } b)}}{\text{Adjusted volume}_{(\text{Displacement distance } b)}} \tag{4}$$

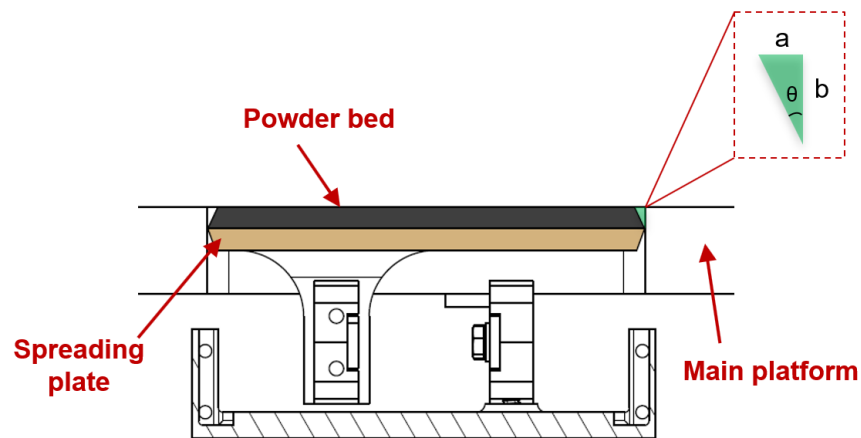


Figure 7. Schematic of the obtained powder bed illustrating the gap between the spreading and main platforms (with «a» the distance between the duct and upper layer and «b» the total spreading plate displacement).

The powder bed density measured using the previously presented method can be validated using cylindrical capsules [25,32] printed while trapping loose powder during a job on a commercial PBAM machine. The trapped powder is collected and weighted and the inner volume of the capsules is estimated to allow the calculation of the powder bed density for a given configuration (powder, spreading parameters, recoating principle). Examples of the obtained powder bed measurement results are presented and compared in Section 5.1.

4.2. Displacements of the Dispensing and Spreading Platforms

The displacement resolution of the dispensing and spreading platforms were assessed using a dial indicator (MITUTOYO Absolute Digimatic, Kanagawa, Japan, resolution 0.001 mm). The motorized platforms were given commands to travel incrementally with repeated displacements ranging between 10 and 400 μm (three times per increment). Figure 8a–c

shows a perfect correlation (slope and R^2 close to unity) between the defined command displacements and the positions measured for both platforms within the 10 to 400 μm range. The average residuals for set displacements are presented in Figure 8b–d and range between $\pm 3 \mu\text{m}$ and $\pm 1.5 \mu\text{m}$ for the dispensing and spreading platforms, respectively.

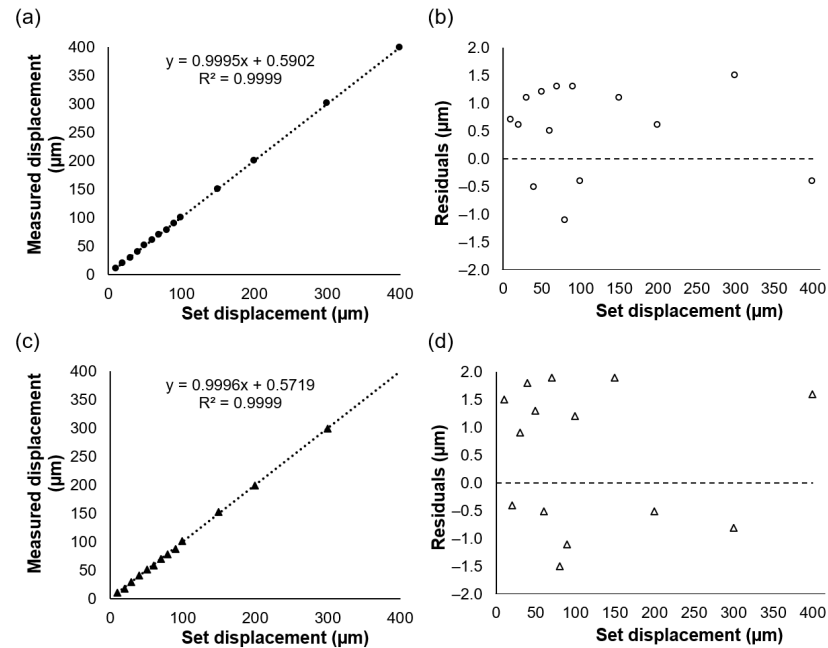


Figure 8. Validation of vertical displacements of the platforms: (a) dispensing platform set versus measured displacements; (b) dispensing platform displacement residuals; (c) spreading platform set versus measured displacements; (d) spreading platform displacement residuals (the error bars are plotted but too small to be visible).

It should be noted that the calibration experiments were executed with no powder present. It is probable that the displacement accuracy of the dispensing platform may be affected by friction caused by fine powder particles that have fallen between the movable and static parts of the bench, although this occurrence is not critical as long as the powder coverage on the spreading platform is sufficient. This problem is, however, irrelevant for the spreading platform thanks to the presence of a 0.1 mm gap between the movable and static parts of the testing apparatus.

4.3. Spreading Forces Measurements

The rotary torque sensor used (TRS605-FSH02054, FUTEK, Irvine, CA, USA) was factory-calibrated to convert the voltage signal (0 to 5 V) into torque values (0 to 5 N·m). Figure 9 shows the calibration graph provided by the manufacturer; reference loads were applied in both rotational directions (clockwise, counterclockwise). The sensor sensitivity and the maximum system error were rated at 0.153 N·mm and $\pm 0.02\%$, respectively.

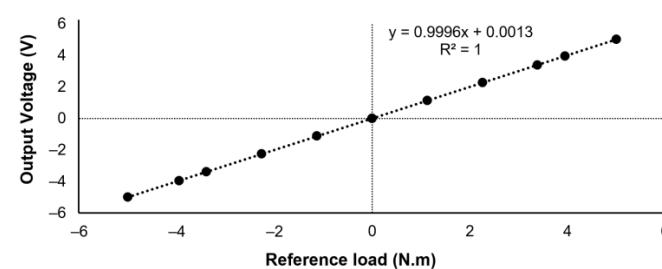


Figure 9. Factory calibration of the rotary torque sensor voltage as a function of the applied load (the error bars are plotted but too small to be visible).

Equation (5) can be used to convert the voltage output into a torque value:

$$\text{Torque measurement(N}\cdot\text{m)} = 1.004 \times \text{Voltage output(V)} - 0.0013, \quad (5)$$

In this work, the torque measurements were recorded with a sampling rate of 1200 Hz. Reference measurements were taken with no powder present (off-load) to assess the torque needed to displace the moving carriage (weight of the components involved, friction with guide rails). The recorded measurements were subtracted from the values obtained with the presence of powder to isolate the torque variations induced by powder spreading.

4.4. Powder Bed Uniformity Assessment

To assess the evenness of the powder bed, a qualitative analysis was carried out using a CCD camera, while a 3D scanner was used to perform a quantitative assessment. To determine the resolution and the smallest detectable features using the CCD, a certified microscope calibration coupon (CL-04-322-850, CLEMEX, Longueuil, QC, Canada) (Figure 10a) was used. Considering the working distance allowing us to capture the full spreading platform, an effective pixel size of 83.3 μm was obtained.

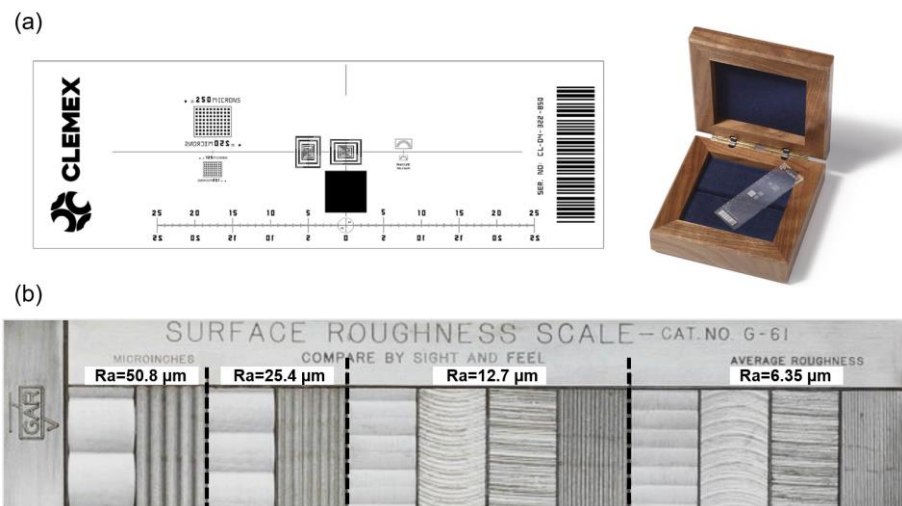


Figure 10. Calibration coupons used: (a) optical microscope calibration coupon; (b) surface roughness calibration coupon.

The 3D scanner captured a point cloud fused and meshed with a pitch of 0.02 mm; to retain the details of the captured surface topography, no noise reduction filter was applied. The file was exported to STL format at a 1:1 scale, cleaned (cropping of unneeded areas, removal of isolated points, filling of holes), and leveled using the area surrounding the spreading platform (main platform; 15 in Figure 1) as a reference. To build the height deviation map, the distance of each point of the spreading area with respect to the mean surface was measured; the mean surface was built using the least squares method. Next, the average height deviation from the mean surface was calculated and used as an indicator of powder bed uniformity.

To estimate the height limitation detectability, calibrated shims with known thicknesses of 40, 50, 60, 70, and 80 μm were placed on a flat substrate, and a dedicated scanning spray coating was applied to render the shim surfaces non-reflective, as shown in Figure 11a. The obtained STL is shown in Figure 11b, where all five shims appear to be detected by the scanner. Figure 11c shows the correlation between the reference and the thicknesses measured using the scanner. The average heights of different areas corresponding to each of the shims with respect to the substrate are estimated using MATLAB. It can be seen that the measured values are higher than the reference, with an average difference of ~6%. The average standard deviation of the measurements was ~2%. The differences in height and

the standard deviations could be explained by the added spray coating, the error induced by the scanner stitching algorithm, the error during the mesh generation, and the error of the STL leveling process with MATLAB. The difference between the thicknesses was statistically significant, and a 10 μm height difference could be detected by the implemented system; thinner shims would, thus, be needed to define the detectability limit of the system.

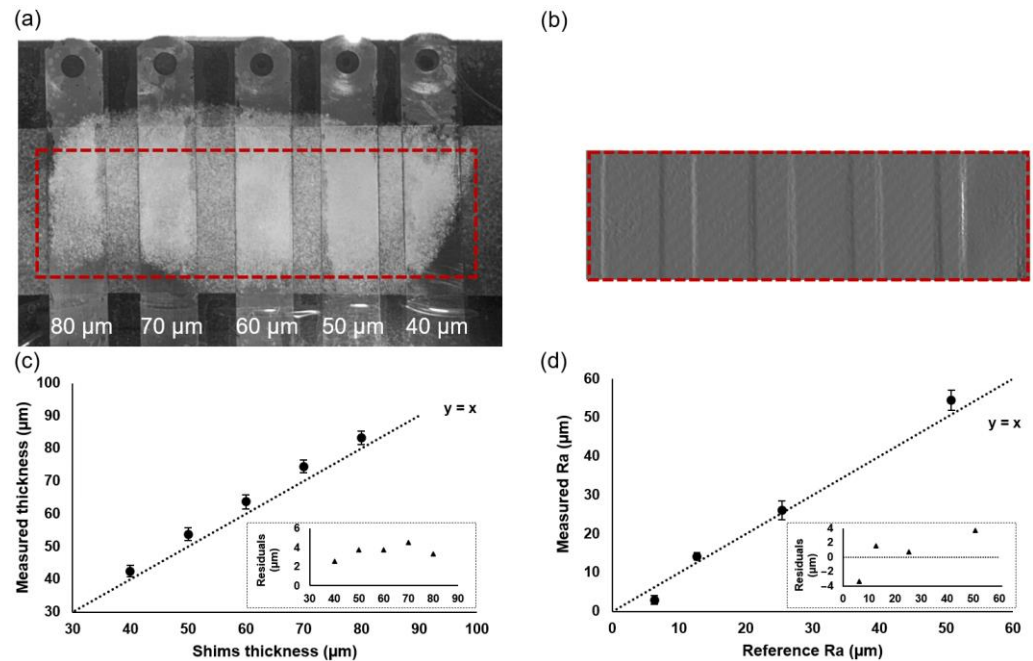


Figure 11. Calibration and validation of the 3D scanner measurements: (a) picture of the selected reference shims; (b) the obtained STL of the reference shims; (c) comparison between the measured and reference thicknesses; (d) correlation between the reference and measured average surface roughnesses of the coupon.

To further validate the obtained results and the developed algorithm, a surface roughness coupon (G61 micro-finish comparator, GAR, Danbury, CT, USA) (Figure 10b) was scanned. The coupon includes indicators for four average surface roughnesses, namely 6.35, 12.7, 25.4, and 50.8 μm. Each indicator was analyzed separately, and the average surface roughness Ra was calculated. The correlations between the reference and measured values are shown in Figure 11d. It can be seen that the implemented system is capable of differentiating the different scanned areas. The trend for the measured values matches the increasing trend of the reference Ra. For the smallest reference Ra 6.35 μm, it seems that the scanner reached its detectability limit and was not able to detect small height variations (−53.6% difference). For the remaining reference values of 12.7, 25.4, and 50.8 μm, the differences were 11.8, 2.7, and 7.2%, respectively.

4.5. Summary of the Powder Spreading Apparatus Characteristics

In summary, the technical characteristics of the powder spreading apparatus are collected in Table 2 for powder spreading and density measurements, in Table 3 for powder spreading and force measurements, and in Table 4 for powder bed uniformity evaluations.

Table 2. Powder spreading and density measurement capabilities.

Powder Dispensing Module		Powder Spreading Mechanism		Weighing Module	
Travel distance (mm)	20	Travel distance (mm)	20	Maximum capacity (g)	465
Dimensions (mm)	120 × 50	Dimensions (mm)	100 × 100	Sensitivity (g)	0.01
Displ. resolution (μm)	10 ± 3	Displ. resolution (μm)	5 ± 1.5	Max. system error (%)	±0.017

Table 3. Spreading arm module and force measurement capabilities.

Spreading Arm Module		Spreading Forces Measurements Module	
Speed range (mm/s)	20–800	Maximum capacity (N·m)	20
Mechanism	Modular, customizable	Sensitivity (N·mm)	100 × 100
Displ. resolution (µm)	10 ± 3	Maximum system error (%)	5 ± 1.5

Table 4. Powder bed uniformity evaluation module capabilities.

Powder Bed Uniformity Evaluation Module	
3D scanner sensitivity (µm)	20
Optical camera resolution (µm)	100 × 100
Evaluated area (mm)	5 ± 1.5

5. Case Study

To demonstrate the technical capabilities of the developed test apparatus, the impact of the layer thickness and recoating speed on the powder bed density, powder bed uniformity, and recoating forces were studied using a Ti-6Al-4V gas-atomized powder supplied by EOS (EOS GmbH, Munich, Germany) (D10 = 25.3, D50 = 35.8 and D90 = 46.4 µm). A single solid flat blade made of Al6061 was used as the spreading tool. The layer thicknesses were 30, 60, and 100 µm (commonly used layer thicknesses on commercial L-PBF machines), while the recoating speeds were 100, 200, 300, 400, and 500 mm/s (commonly used recoating speeds on commercial L-PBF machines range from XX to YY). To ensure a constant range of measuring sensitivities during the entire study, the total spreading platform displacement for each of the testing cases was kept constant and equal to 1.2 mm, which required 40 layers of powder for a layer thickness of 30 µm, 20 layers of powder for a layer thickness of 60 µm, and 12 layers of powder for a layer thickness of 100 µm. The increment displacement of the dispensing platform (the charge amount) was 500% of the spreading platform displacement increment (the layer thickness), as described by Equation (1) in Section 2.1. This value was defined considering differences in the respective surface areas of the dispensing and spreading platforms, as well as to compensate for the powder losses due to the presence of a gap around the spreading platform. For each layer spread, the masses of the deposited powder and spreading forces were recorded. Additional powder bed uniformity measurements were performed after the last layer of powder was deposited.

The results obtained using the different measurement modules are presented and discussed in the next sections in the order of the powder bed density, powder spreading forces, and powder bed uniformity. The results obtained with the testing apparatus of the present study are then compared with data obtained from literature sources and from additional experiments using different measurement techniques.

5.1. Powder Bed Density

The average powder bed density was calculated by evaluating the average deposited mass per layer divided by the adjusted volume and normalized by the theoretical density of Ti-6Al-4V (4.41 g/cm³). The bulk properties (tapped and apparent density levels of the feedstock powder) and the powder bed density determined using the printed capsule method [32] were used as reference data. The obtained results are reported in Figure 12 and in Table A2 (Appendix C). Regarding the measurements performed using the test apparatus, it can be seen that the greater the layer thickness and the higher the recoating speed, the lower the powder bed density.

For example, for a recoating speed of 100 mm/s, the highest density of 60 ± 2% was obtained for a layer thickness of 30 µm, which was respectively 2.6 and 6.6% higher than the powder bed densities obtained for the 60- and 100-µm-thick layers. Moreover, for the layer thickness of 30 µm, the highest density was obtained with a recoating speed of 100 mm/s, which was respectively 2.6, 12.4, 12.8, and 24.9% higher than the powder bed densities obtained with recoating speeds of 200, 300, 400, and 500 mm/s. A trend can also be seen in

the standard deviations of the results obtained, where an increase in the layer thickness and in the recoating speed was accompanied by an increase in the results' variability. This variability could also be related to inconsistent powder collapse in the neighboring area of the gap, where powder can accumulate (increased deposited mass) and collapse once the avalanche angle of the powder is reached (loss in deposited mass). Note that for the same layer thicknesses of 30 and 60 μm , the difference between the Ti-6Al-4V powder bed densities of this study for a recoating speed of 100 mm/s and those obtained by the printed capsule method [32] (recoating speed 80 mm/s) was less than 1%.

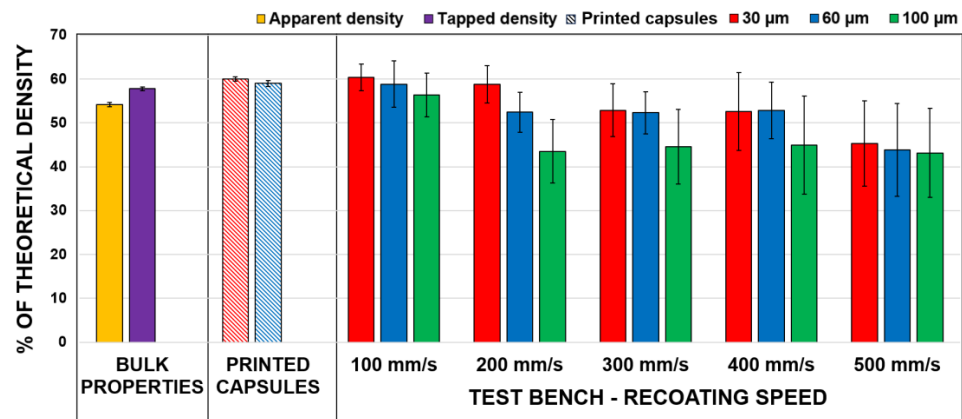


Figure 12. Powder bed density as a function of the layer thickness and recoating speed with the reference values (bulk properties and printed capsule densities [32]).

5.2. Spreading Forces

The torque variations of the recoating arm actuator were measured during the test sequence. For each recoating speed, reference measurements were taken without powder to evaluate the system-induced torque variations. The torque value was divided by the drive pulley radius of 12.75 mm and the width of the spreading blade to evaluate the spreading forces per contact length of 120 mm. The obtained results are reported in Figure 13 and Table A3 (Appendix C). A reference value obtained using the shear cell testing mode of an FT4 powder rheometer is also included [32]. It can be seen that in most cases, the greater the layer thickness and the higher the recoating speed, the higher the spreading forces. The reference (rheometer) value is within the same order of magnitude as the measurements performed with the test apparatus; it should be noted that the rheometer tests the powder in a compacted state.

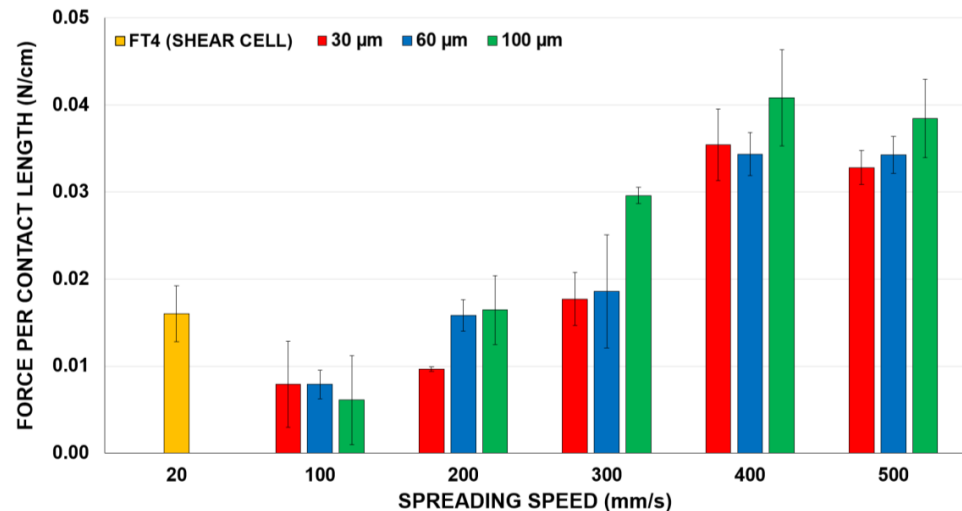
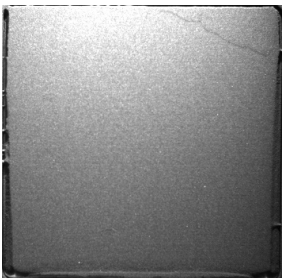
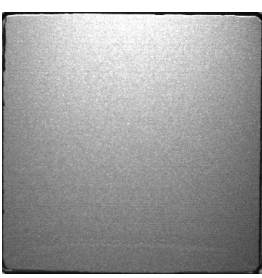
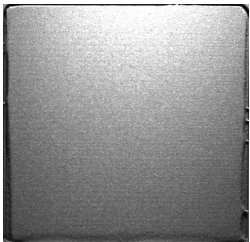
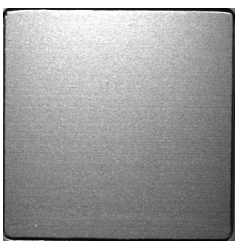
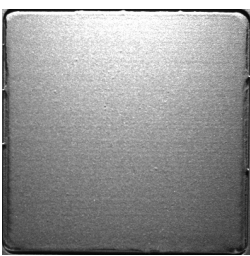
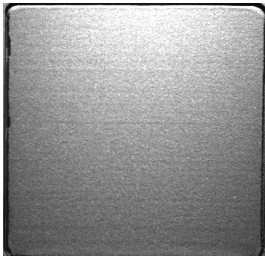
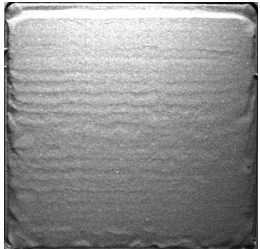
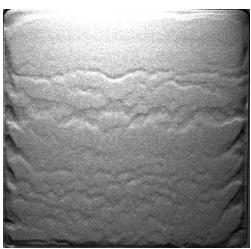


Figure 13. Spreading forces as functions of the layer thickness and the recoating speed.

5.3. Powder Bed Uniformity

The powder bed uniformity was assessed on the last spread layer of the test sequence. Table 5 includes pictures captured using a CCD camera installed above the spreading platform to allow a qualitative inspection of the powder bed uniformity.

Table 5. Powder bed images for different layer thicknesses and recoating speeds.

Recoating Speed (mm/s)	Layer Thickness (μm)		
	30	60	100
100			
200			
300			
400			
500			

Based on the powder bed pictures for the three studied layer thicknesses (Table 5), significant turbulences of the powder bed occur starting at a recoating speed of 400 mm/s. For the lower speeds, no major turbulences or significant differences between the studied cases can be detected based on the qualitative evaluation performed (Table 5).

For the quantitative assessment, representations of the powder bed were captured using a blue light 3D scanner. The point cloud obtained were cleaned, leveled, and the distance of each of the points from the plan fitted using the least squares method were measured to build the height deviation maps shown in Figure 14. The average height deviations for the different layer thicknesses and recoating speeds are reported in Figure 15. As shown in the figure, the height deviations for the two fastest recoating speeds of 400 and 500 mm/s are significantly greater, given the presence of pronounced turbulences on the powder bed. For the recoating speeds of 100, 200, and 300 mm/s, noticeably smaller height deviations were observed, with the impact of the recoating speed on the powder bed uniformity for these configurations being almost negligible.

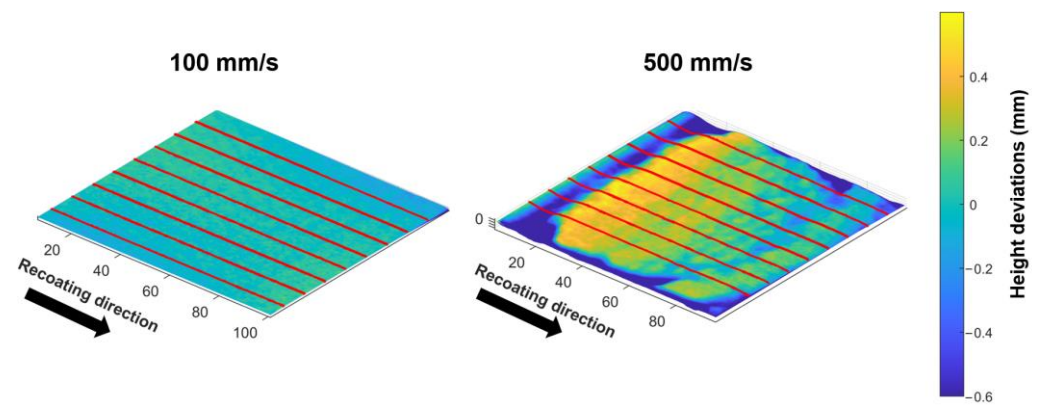


Figure 14. Powder bed height deviations for spreading speeds of 100 and 500 mm/s and a layer thickness of 100 μm .

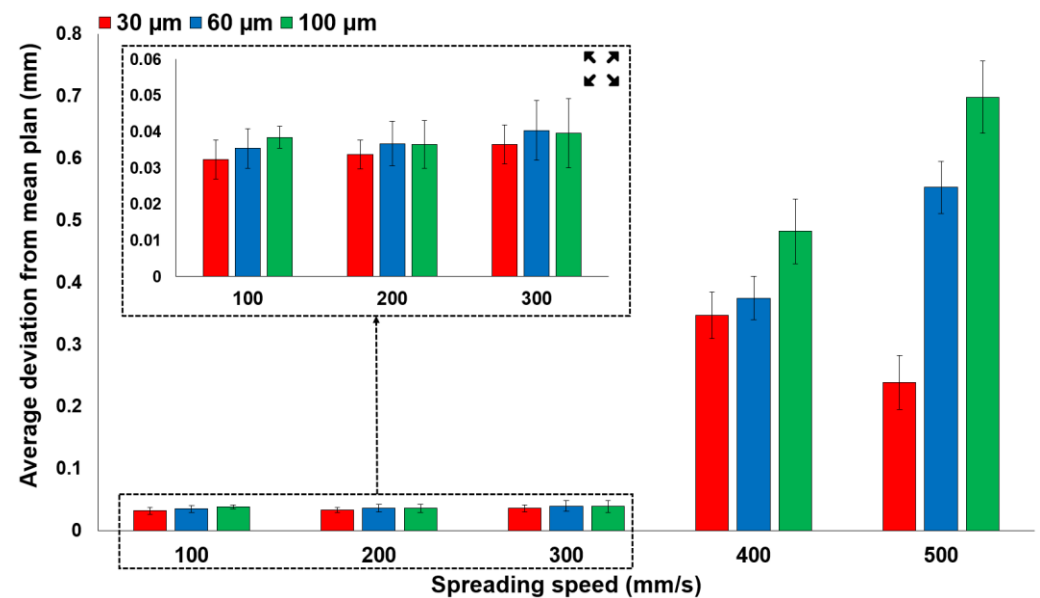


Figure 15. Powder bed average height deviations as functions of the layer thickness and the spreading speed.

A high-resolution KEYENCE VR-5000 3D scanner (0.1 μm resolution) using blue laser scanning technology and a high-accuracy CMOS sensor were used to obtain reference values for the powder bed height deviations. The same powder considered in the case

study was manually spread (speed unquantified ~80–100 mm/s) using a scraper on a flat coupon with an 8 mm depth recess. The obtained powder bed was analyzed with a high-resolution 3D scanner (KEYENCE VR-5000) and the height deviations were within the ± 40 μm range, which was in agreement with the deviation range measured by the scanning system of this testing apparatus (REVOPOINT MINI).

5.4. Discussion of the Case Study

The differences in the powder bed densities for different layer thicknesses and recoating speeds (Figures 12 and 15) may be partly attributable to variations in the particle size distributions (PSDs) between the dispensing and spreading platforms and the powder collector caused by powder spreading [25,36,55]. To verify this hypothesis, powder samples were taken along the spreading path from the dispensing platform to the spreading platform and finally to the collector for 3 layer thicknesses and 5 recoating speeds. The PSDs of the collected samples were measured using a laser diffraction particle size analyzer (Beckman Coulter LS XR 13-320).

As an example, the PSDs of the powder deposited on the spreading platform using the same recoating speed of 300 mm/s but three different layer thicknesses are shown in Figure 16a and compared to the reference PSD (dispenser). It can be seen that the smaller the layer thickness, the more the PSD on the spreading platform is shifted towards smaller particles, most probably because when the gap between the blade and the platform becomes smaller, the number of larger particles dragged by the blade to the collector becomes greater. The same phenomenon could explain an increase in the powder bed density with a decrease in the layer thickness (Figure 12), since finer particles remaining on the spreading platform fill the existing gaps within the powder bed more efficiently [25,36,55]. This is also confirmed by the results reported in Figure 16b–d showing PSD variations of the powder samples taken along the spreading direction, whereby the greater the layer thickness, the smaller the number of larger particles dragged from the dispenser to the collector.

The PSDs measured on the spreading platform are also influenced by the recoating speed variations, and an example of such an influence can be seen in Figure 17 for a constant layer thickness of 100 μm . It can be seen that when the recoating speed increases from 100 to 200 and 300 mm/s, the PSD on the spreading platform shifts towards larger particles (increases in D10, D50, and D90), which can be explained as follows. The higher the spreading speed, the shorter the available settling time for smaller particles within the gaps of a powder bed. The scraper travel speed has an effect on the particle mass flow in the gap between the scraper and the underlying layer. This increases linearly with the blade speed until a critical speed is reached, where the mass flow rate reaches an asymptotic value representing the maximum deposition rate that can be achieved for a given spacing. At low recoating speeds, the inertial time scale of the spreading is longer than the inertial time scale of gravity, and consequently particles have time to fall and pass through the gap. On the other hand, at high recoating velocities, when the inertial time scale of the spreading is much shorter than the inertial time scale of gravity, particles cannot fall through the gap fast enough, limiting the particle deposition (mass flow) [6,56,57]. The same powder coarsening phenomenon can also explain a decrease in the powder bed density with an increase in the spreading speed reported in Figure 12. This trend is inverted when the recoating speeds reach 400 and 500 mm/s, whereby the PSDs on the spreading platform then shift towards finer particles. A decrease in the powder bed density in this case is associated with a lack of powder coverage, which can be observed in Figure 14 (uneven powder bed).

The surface profile of the spread layer can also be correlated with the powder bed density, whereby a tightly packed bed produces a surface with fewer discontinuities, which could explain the results presented for powder bed average height deviations as functions of the layer thickness for spreading speeds of 100, 200, and 300 mm/s in Figure 15 [36,58–60].

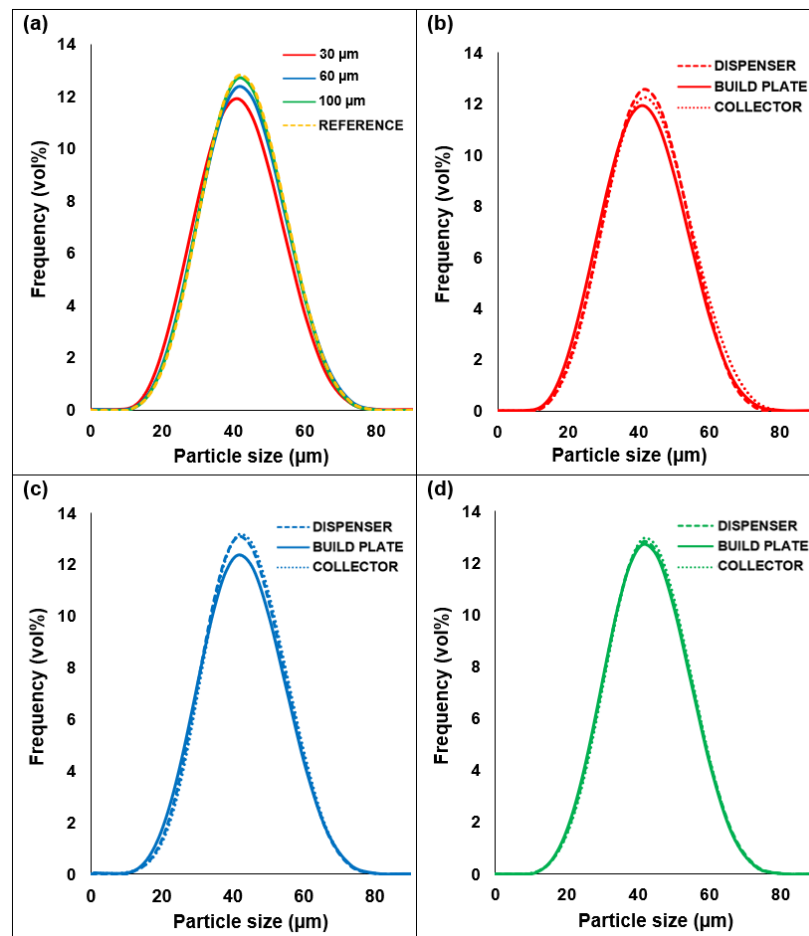


Figure 16. PSD variations for a constant recoating speed of 300 mm/s: (a) PSDs on the spreading platform as functions of the layer thickness; PSDs along the spreading path as functions of the layer thickness of (b) 30 μm, (c) 60 μm, and (d) 100 μm.

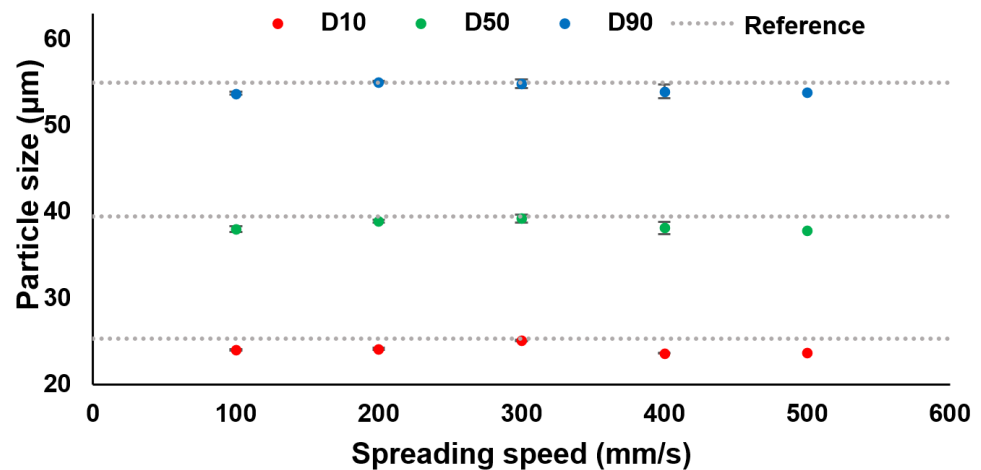


Figure 17. PSD variations on the spreading platform as functions of the recoating speed for a layer thickness of 100 μm.

The increase in the spreading forces with an increase in the layer thickness (Figure 13) can be explained by a greater amount of powder being displaced (charge amount %) and greater particle–particle frictional interactions. Higher recoating speeds increase the particle circulation within the heap in front of the blade, enhancing the convection motion and interaction with particles of the underlying powder bed and increasing the cohesive forces

present in the powder cluster [53,61,62]. These phenomena favor a random formation of the force arches and intermittent particle blockages reducing the powder passage cross-section. The formation and breakage of these force arches generate random fluctuations in particle stresses and variable flow conditions during powder bed spreading [63,64]. The recoating forces and particles dynamics involved during the spreading highly impact the surface uniformity of the powder bed, whereby the enhanced convective motion of the particle heap in front of the blade and the increased interaction with the previously deposited particles can create disturbances, as observed in Figure 13 for spreading speeds of 400 and 500 mm/s.

6. Conclusions

In this work, the design, calibration, and validation of a novel testing apparatus (Figures 1 and A1) reproducing the main components involved in the powder spreading operation of commercial PBAM machines was presented. This apparatus offers customizable powder spreading settings (layer thickness, spreading speed, and design of the spreading mechanism) and allows measurements of relevant powder spreading metrics (powder bed density, uniformity, and spreading forces). Furthermore, a case study was carried out to demonstrate the technical capabilities of the developed test apparatus, and the impacts of the layer thickness and recoating speed on the powder bed density, powder bed uniformity, and recoating forces were studied using a typical Ti-6Al-4V gas-atomized powder. The results obtained were compared with the literature and we confirmed the overall validity of the observations made with the proposed testing apparatus. Future work using the proposed testing apparatus will be focused on the impact of the intrinsic characteristics of the powders (chemical composition, particle size, and morphology) compounded with the powder spreading conditions and the effects on the powder bed density, uniformity, and spreading forces. Based on the result of this study, prior to the optimization of laser bed fusion parameters, the powder density and uniformity could be maximized and the spreading forces minimized, with the ultimate objective of establishing the best trade-off between the process productivity (minimum recoating time) and mechanical and geometric service properties of the printed components.

Author Contributions: Conceptualization, S.E.B. and V.B.; methodology, S.E.B. and V.B.; software, S.E.B. validation, S.E.B. and V.B.; formal analysis, S.E.B. and V.B.; investigation, S.E.B. and V.B.; resources, V.B.; data curation, S.E.B. and V.B.; writing—original draft preparation, S.E.B.; writing—review and editing, S.E.B. and V.B.; visualization, S.E.B.; supervision, V.B.; project administration, V.B.; funding acquisition, V.B. All authors have read and agreed to the published version of the manuscript.

Funding: The financial support of the Natural Sciences and Engineering Research Council of Canada (NSERC) is gratefully acknowledged (NSERC Discovery Grant RGPIN-2020-05800).

Data Availability Statement: Data or material related to this study are available on request from the corresponding author.

Acknowledgments: The authors would like to express their appreciation for the support provided by M. Drouin and O. Bourdeau-Rousseau and to thank M. Samoilenko, A. Timercan, M. Letenneur, and W. Turnier Trottier for their assistance during this project.

Conflicts of Interest: The authors declare no conflict of interest.

Appendix A. Control Architecture

The front panel of the apparatus shown on 13 in Figure 1 and the front view of Figure A1 allows the operator to control the different modules of the test bench and define the test settings. Figure A2 shows the control panel and Table A1 lists and describes the elements of the panel.



Figure A1. Pictures of the testing apparatus.

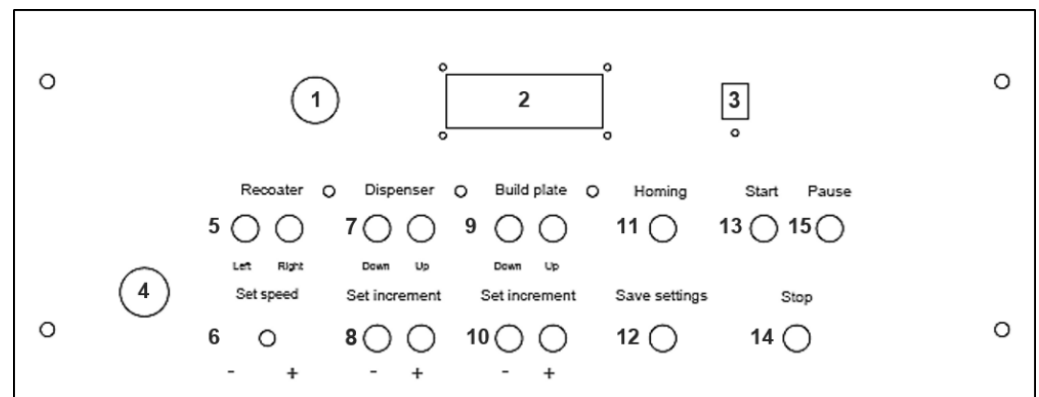


Figure A2. Control panel layout.

Table A1. List and description of the control panel elements.

N°	Item	Description
1	ON/OFF button	Button to switch on and off the test bench
2	LCD screen	Screen to display the recoating speed, increment settings, temperature, humidity, and test status
3	Temperature and humidity sensor	DHT11 sensor to monitor the temperature and humidity during the test
4	Emergency stop button	Button to shut off the test in case of emergency
5	Spreading arm control	Buttons to control the movements of the spreading arm horizontally (right and left)
6	Spreading speed setting	Potentiometer to control the spreading arm’s speed of advance (recoating speed)
7	Dispensing platform control	Buttons to control the movements of the dispensing platform vertically (up and down)
8	Dispensing increment control	Defines the increment of the dispensing platform displacement (+ and –)
9	Spreading platform control	Buttons to control the movements of the spreading platform vertically (up and down)
10	Spreading platform increment control	Defines the increment of the spreading platform displacements (+ and –)
11	Homing button	Button to bring back the different moving elements of the test bench to their initial positions (safe positions)
12	Save settings	Button to save the defined settings (recoating speed, dispensing and spreading platforms’ increments) on the internal memory of the microcontroller
13	Start test button	Button to start the test sequence defined in Section 3
14	Stop test button	Button to stop the test sequence (test progress is lost)
15	Pause test button	Button to pause the test sequence (test sequence is on hold until the start button is pressed again)

Figure A3 shows a simplified schematic of the electrical connections and communications between the main components of the apparatus. The ARDUINO MEGA 2560 microcontroller is used for the control of the dispensing and spreading platform modules' displacements, the load cells readings, and interactions with the control panel components and limit switches, in addition to the communication with the DMC31012 spreading mechanism motor controller to synchronize the displacement sequence of the modules involved in the spreading operation. The CCD camera is connected via a network interface card; the DMC31012 controller uses an ethernet connection; and the Arduino board, the 3D scanner, and the torque sensor are connected via a universal serial board to a centralized computer where the dedicated software packages are installed and used to edit the spreading parameters and display and record the sensors readings.

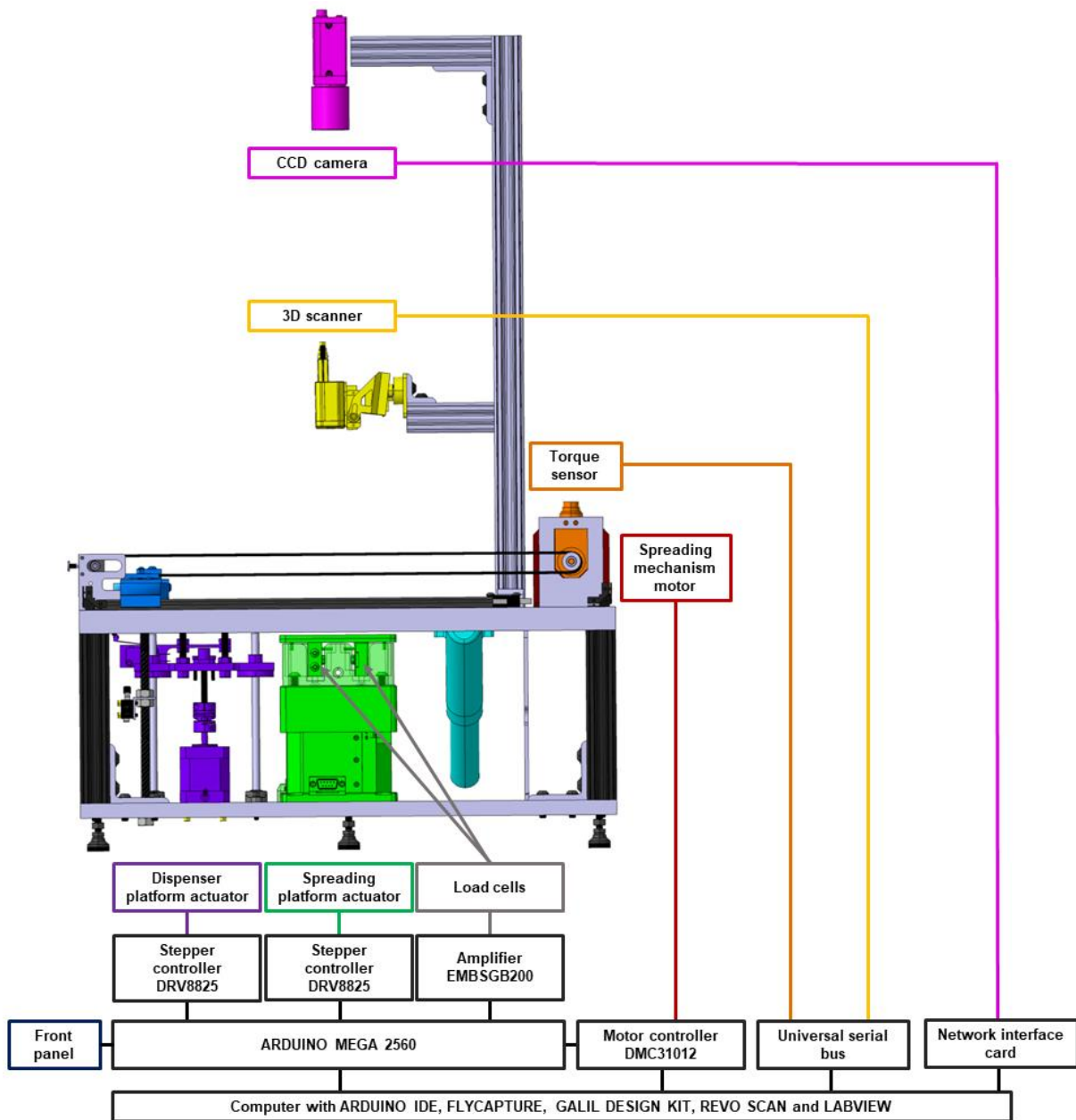


Figure A3. Simplified electronic wiring and communication schematic of the apparatus.

Appendix B. Detailed Testing Procedure

Figure A4 presents a diagram of the detailed test sequence of the proposed apparatus.

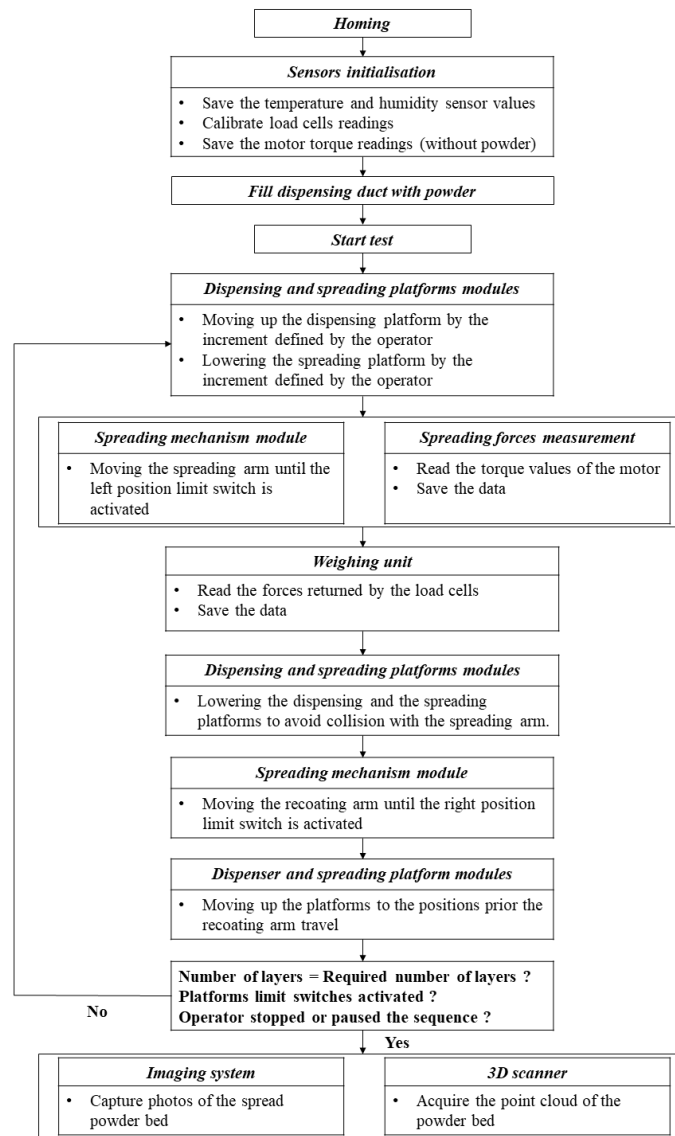


Figure A4. Test sequence of the powder spreading apparatus.

Appendix C. Detailed Results

Table A2. Powder bed density values as a function of the layer thickness and recoating speed with reference values (bulk properties and printed capsules densities).

Layer Thickness, μm	30	60	100	NA
Test apparatus measurements				
Powder bed density (%) for a recoating speed (mm/s) of:				
100	60.4 ± 3.1	58.8 ± 5.3	56.4 ± 5.0	--
200	58.8 ± 4.3	52.4 ± 4.5	43.5 ± 7.3	--
300	52.9 ± 6.0	52.3 ± 4.8	44.6 ± 8.5	--
400	52.6 ± 8.9	52.8 ± 6.4	44.9 ± 11.2	--
500	45.3 ± 9.7	43.8 ± 10.6	43.1 ± 10.1	--
Printed capsules measurements [32]				
Powder bed density (%) for a recoating speed 80 mm/s	60.0 ± 0.5	59.0 ± 0.7	--	--
Bulk properties				
Apparent density (%)	--	--	--	54.2 ± 0.003
Tapped density (%)	--	--	--	57.8 ± 0.005

Table A3. Spreading forces as functions of the layer thickness and recoating speed.

Layer Thickness, μm	30	60	100	NA
Test bench measurements				
Spreading force per contact length (N/cm) for a recoating speed (mm/s) of:				
100	0.008 ± 0.005	0.008 ± 0.002	0.006 ± 0.005	--
200	0.010 ± 0.001	0.016 ± 0.002	0.016 ± 0.004	--
300	0.018 ± 0.003	0.019 ± 0.006	0.030 ± 0.001	--
400	0.035 ± 0.004	0.034 ± 0.002	0.041 ± 0.006	--
500	0.033 ± 0.002	0.034 ± 0.002	0.038 ± 0.004	--
FT4 rheometer (shear cell) (N/cm)				
for a shearing speed of 20 mm/s				
	--	--	--	0.016 ± 0.003

References

1. Wohlers, T.; Associates, W.; Campbell, R.I.; Diegel, O.; Huff, R.; Kowen, J. *Wohlers Report 2020: 3D Printing and Additive Manufacturing State of the Industry*; Wohlers Associates: Washington DC, USA, 2020.
2. Popov, V.V.; Grilli, M.L.; Koptuyug, A.; Jaworska, L.; Katz-Demyanetz, A.; Klobčar, D.; Balos, S.; Postolnyi, B.O.; Goel, S. Powder Bed Fusion Additive Manufacturing Using Critical Raw Materials: A Review. *Materials* **2021**, *14*, 909. [[PubMed](#)]
3. Bhavar, V.; Kattire, P.; Patil, V.; Khot, S.; Gujar, K.; Singh, R. A review on powder bed fusion technology of metal additive manufacturing. In *Additive Manufacturing Handbook*; Routledge Taylor & Francis Group: London, UK, 2017; pp. 251–253.
4. Yadroitsev, I.; Yadroitsava, I. A step-by-step guide to the L-PBF process. In *Fundamentals of Laser Powder Bed Fusion of Metals*; Elsevier: Amsterdam, The Netherlands, 2021.
5. Haeri, S. Optimisation of blade type spreaders for powder bed preparation in Additive Manufacturing using DEM simulations. *Powder Technol.* **2017**, *321*, 94–104. [[CrossRef](#)]
6. Haeri, S.; Wang, Y.; Ghita, O.; Sun, J. Discrete element simulation and experimental study of powder spreading process in additive manufacturing. *Powder Technol.* **2017**, *306*, 45–54. [[CrossRef](#)]
7. Budding, A.; Vaneker, T.H.J. New Strategies for Powder Compaction in Powder-based Rapid Prototyping Techniques. *Procedia CIRP* **2013**, *6*, 527–532. [[CrossRef](#)]
8. Wang, L.; Yu, A.; Li, E.; Shen, H.; Zhou, Z. Effects of spreader geometry on powder spreading process in powder bed additive manufacturing. *Powder Technol.* **2021**, *384*, 211–222. [[CrossRef](#)]
9. Yang, L.; Hsu, K.; Baughman, B.; Godfrey, D.; Medina, F.; Menon, M.; Wiener, S. *Additive Manufacturing of Metals: The Technology, Materials, Design and Production*; Springer: Berlin/Heidelberg, Germany, 2017.
10. Zhang, J.; Tan, Y.; Bao, T.; Xu, Y.; Xiao, X.; Jiang, S. Discrete Element Simulation of the Effect of Roller-Spreading Parameters on Powder-Bed Density in Additive Manufacturing. *Materials* **2020**, *13*, 2285. [[CrossRef](#)] [[PubMed](#)]
11. Daňa, M.; Zetková, I.; Hanzl, P. The Influence of a Ceramic Recoater Blade on 3D Printing using Direct Metal Laser Sintering. *Manuf. Technol.* **2019**, *19*, 23–28. [[CrossRef](#)]
12. Kayacan, M.Y.; Özsoy, K.; Duman, B.; Yilmaz, N.; Kayacan, M.C. A study on elimination of failures resulting from layering and internal stresses in Powder Bed Fusion (PBF) additive manufacturing. *Mater. Manuf. Process.* **2019**, *34*, 1467–1475. [[CrossRef](#)]
13. Shamsdini, S.; Ghoncheh, M.H.; Mohammadi, M. Effect of recoater-blade type on the mechanical properties and microstructure of additively manufactured maraging steels. *Mater. Sci. Eng. A* **2021**, *812*, 141104. [[CrossRef](#)]
14. Ziaee, M.; Crane, N.B. Binder jetting: A review of process, materials, and methods. *Addit. Manuf.* **2019**, *28*, 781–801.
15. Mostafaei, A.; Elliott, A.M.; Barnes, J.E.; Li, F.; Tan, W.; Cramer, C.L.; Nandwana, P.; Chmielus, M. Binder jet 3D printing—Process parameters, materials, properties, modeling, and challenges. *Prog. Mater. Sci.* **2021**, *119*, 100707.
16. Mirzababaei, S.; Pasebani, S. A review on binder jet additive manufacturing of 316L stainless steel. *J. Manuf. Mater. Process.* **2019**, *3*, 82.
17. Oropeza, D.; Roberts, R.; Hart, A.J. A modular testbed for mechanized spreading of powder layers for additive manufacturing. *Rev. Sci. Instrum.* **2021**, *92*, 015114. [[CrossRef](#)]
18. Oropeza, D.; Penny, R.W.; Gilbert, D.; Hart, A.J. Mechanized spreading of ceramic powder layers for additive manufacturing characterized by transmission X-ray imaging: Influence of powder feedstock and spreading parameters on powder layer density. *Powder Technol.* **2022**, *398*, 117053. [[CrossRef](#)]
19. Foster, B.; Reutzler, E.; Nassar, A.; Hall, B.; Brown, S.; Dickman, C. Optical, layerwise monitoring of powder bed fusion. In Proceedings of the Solid Freeform Fabrication Symposium, Austin, TX, USA, 10 August 2015; pp. 10–12.
20. Vlasea, M.L.; Lane, B.; Lopez, F.; Mekhontsev, S.; Donmez, A. Development of powder bed fusion additive manufacturing test bed for enhanced real-time process control. In Proceedings of the International Solid Freeform Fabrication Symposium, Austin, TX, USA, 10 August 2015; pp. 13–15.
21. Kolossov, S.; Boillat, E.; Glardon, R.; Fischer, P.; Locher, M. 3D FE simulation for temperature evolution in the selective laser sintering process. *Int. J. Mach. Tools Manuf.* **2004**, *44*, 117–123.

22. Gusarov, A.; Yadroitsev, I.; Bertrand, P.; Smurov, I. Model of radiation and heat transfer in laser-powder interaction zone at selective laser melting. *J. Heat Transf.* **2009**, *131*, 072101.
23. Patil, R.B.; Yadava, V. Finite element analysis of temperature distribution in single metallic powder layer during metal laser sintering. *Int. J. Mach. Tools Manuf.* **2007**, *47*, 1069–1080.
24. Matsumoto, M.; Shiomi, M.; Osakada, K.; Abe, F. Finite element analysis of single layer forming on metallic powder bed in rapid prototyping by selective laser processing. *Int. J. Mach. Tools Manuf.* **2002**, *42*, 61–67.
25. Jacob, G.; Jacob, G.; Brown, C.U.; Donmez, A. *The Influence of Spreading Metal Powders with Different Particle Size Distributions on the Powder Bed Density in Laser-Based Powder Bed Fusion Processes*; U.S. Department of Commerce, National Institute of Standards and Technology: Gaithersburg, MD, USA, 2018.
26. Brika, S.E.; Zhao, Y.F.; Brochu, M.; Mezzetta, J. Multi-objective build orientation optimization for powder bed fusion by laser. *J. Manuf. Sci. Eng.* **2017**, *139*, 111011.
27. Baumers, M.; Tuck, C.; Wildman, R.; Ashcroft, I.; Rosamond, E.; Hague, R. Combined build-time, energy consumption and cost estimation for direct metal laser sintering. In Proceedings of the Twenty Third Annual International Solid Freeform Fabrication Symposium—An Additive Manufacturing Conference, Austin, TX, USA, 15 August 2012.
28. Piili, H.; Happonen, A.; Väistö, T.; Venkataraman, V.; Partanen, J.; Salminen, A. Cost estimation of laser additive manufacturing of stainless steel. *Phys. Procedia* **2015**, *78*, 388–396.
29. Seyda, V.; Herzog, D.; Emmelmann, C. Relationship between powder characteristics and part properties in laser beam melting of Ti-6Al-4V, and implications on quality. *J. Laser Appl.* **2017**, *29*, 022311.
30. Chen, G.; Zhao, S.; Tan, P.; Wang, J.; Xiang, C.; Tang, H. A comparative study of Ti-6Al-4V powders for additive manufacturing by gas atomization, plasma rotating electrode process and plasma atomization. *Powder Technol.* **2018**, *333*, 38–46.
31. Brika, S.E.; Brailovski, V. Influence of Powder Particle Morphology on the Static and Fatigue Properties of Laser Powder Bed-Fused Ti-6Al-4V Components. *J. Manuf. Mater. Process.* **2020**, *4*, 107.
32. Brika, S.E.; Letenneur, M.; Dion, C.A.; Brailovski, V. Influence of particle morphology and size distribution on the powder flowability and laser powder bed fusion manufacturability of Ti-6Al-4V alloy. *Addit. Manuf.* **2020**, *31*, 100929.
33. Spierings, A.B.; Levy, G. Comparison of density of stainless steel 316L parts produced with selective laser melting using different powder grades. In Proceedings of the Annual International Solid Freeform Fabrication Symposium, Austin, TX, USA, 15 September 2009; pp. 342–353.
34. Spierings, A.B.; Herres, N.; Levy, G. Influence of the particle size distribution on surface quality and mechanical properties in AM steel parts. *Rapid Prototyp. J.* **2011**, *17*, 195–202.
35. Badrossamay, M.; Yasa, E.; Van Vaerenbergh, J.; Kruth, J.-P. Improving productivity rate in SLM of commercial steel powders. *Tech. Pap. Soc. Manuf. Eng.* **2009**, *13*, 1–13.
36. Abd-Elghany, K.; Bourell, D. Property evaluation of 304L stainless steel fabricated by selective laser melting. *Rapid Prototyp. J.* **2012**, *18*, 420–428.
37. Liu, B.; Wildman, R.; Tuck, C.; Ashcroft, I.; Hague, R. Investigation the effect of particle size distribution on processing parameters optimisation in selective laser melting process. In Proceedings of the 2011 International Solid Freeform Fabrication Symposium, Austin, TX, USA, 8 August 2011.
38. Lutter-Günther, M.; Horn, M.; Seidel, C.; Reinhart, G. Influence of Particle Size Distribution on Powder Flowability and Part Properties in Laser Beam Melting: Einfluss der Korngrößenverteilung auf Fließfähigkeit und Bauteilqualität beim Laserstrahlschmelzen. In Proceedings of the Rapid. Tech—International Trade Show & Conference for Additive Manufacturing, Proceedings of the 14th Rapid. Tech Conference, Erfurt, Germany, 20 June 2017; pp. 20–22.
39. Baitimerov, R.; Lykov, P.; Zhrebtsov, D.; Radionova, L.; Shultc, A.; Prashanth, K.G. Influence of powder characteristics on processability of AlSi12 alloy fabricated by selective laser melting. *Materials* **2018**, *11*, 742.
40. Ahmed, M.; Pasha, M.; Nan, W.; Ghadiri, M. A simple method for assessing powder spreadability for additive manufacturing. *Powder Technol.* **2020**, *367*, 671–679.
41. Beitz, S.; Uerlich, R.; Bokelmann, T.; Diener, A.; Vietor, T.; Kwade, A. Influence of powder deposition on powder bed and specimen properties. *Materials* **2019**, *12*, 297. [[PubMed](#)]
42. Cordova, L.; Bor, T.; de Smit, M.; Campos, M.; Tinga, T. Measuring the spreadability of pre-treated and moisturized powders for laser powder bed fusion. *Additive Manuf.* **2020**, *32*, 101082.
43. Lefebvre, L.; Dai, J.; Thomas, Y.; Martinez-Rubi, Y. Metal powder flowability: Effect of humidity and impact on the reproducibility of the measurements. In Proceedings of the Additive Manufacturing with Powder Metallurgy Conference, Phoenix, AZ, USA, 23 June 2019.
44. Le, T.-P.; Wang, X.; Davidson, K.P.; Fronda, J.E.; Seita, M. Experimental analysis of powder layer quality as a function of feedstock and recoating strategies. *Addit. Manuf.* **2021**, *39*, 101890.
45. Hulme-Smith, C.N.; Hari, V.; Mellin, P. Spreadability Testing of Powder for Additive Manufacturing. *BHM Berg-Und Hüttenmännische Mon.* **2021**, *166*, 9–13.
46. Lee, Y.; Simunovic, S.; Gurnon, K.A. *Quantification of Powder Spreading Process for Metal Additive Manufacturing*; Oak Ridge National Lab. (ORNL): Oak Ridge, TN, USA, 2019.
47. Snow, Z.K. Understanding Powder Spreadability in Powder Bed Fusion Additive Manufacturing. Master's Thesis, The Pennsylvania State University, State College, PA, USA, 2018.

48. Van den Eynde, M.; Verbelen, L.; Van Puyvelde, P. Assessing polymer powder flow for the application of laser sintering. *Powder Technol.* **2015**, *286*, 151–155.
49. Mehrabi, M.; Gardy, J.; Talebi, F.A.; Farshchi, A.; Hassanpour, A.; Bayly, A.E. An investigation of the effect of powder flowability on the powder spreading in additive manufacturing. *Powder Technol.* **2023**, *413*, 117997. [[CrossRef](#)]
50. Lupo, M.; Ajabshir, S.Z.; Sofia, D.; Barletta, D.; Poletto, M. Experimental metrics of the powder layer quality in the selective laser sintering process. *Powder Technol.* **2023**, *419*, 118346. [[CrossRef](#)]
51. Mitterlehner, M.; Danninger, H.; Gierl-Mayer, C.; Gschiel, H. Investigation of the Influence of Powder Moisture on the Spreadability Using the Spreading Tester. *BHM Berg Hüttenmännische Mon.* **2021**, *166*, 14–22.
52. Yee, I. Powder Bed Surface Quality and Particle Size Distribution for Metal Additive Manufacturing and Comparison with Discrete Element Model. Master's Thesis, California Polytechnic State University, San Luis Obispo, CA, USA, 2018.
53. Escano, L.I.; Parab, N.D.; Xiong, L.; Guo, Q.; Zhao, C.; Fezzaa, K.; Everhart, W.; Sun, T.; Chen, L. Revealing particle-scale powder spreading dynamics in powder-bed-based additive manufacturing process by high-speed x-ray imaging. *Sci. Rep.* **2018**, *8*, 15079.
54. Lhuissier, P.; Bataillon, X.; Maestre, C.; Sijobert, J.; Cabrol, E.; Bertrand, P.; Boller, E.; Rack, A.; Blandin, J.-J.; Salvo, L. In situ 3D X-ray microtomography of laser-based powder-bed fusion (L-PBF)—A feasibility study. *Addit. Manuf.* **2020**, *34*, 101271.
55. Ali, U.; Mahmoodkhani, Y.; Shahabad, S.I.; Esmailizadeh, R.; Liravi, F.; Sheydaeian, E.; Huang, K.Y.; Marzbanrad, E.; Vlasea, M.; Toyserkani, E. On the measurement of relative powder-bed compaction density in powder-bed additive manufacturing processes. *Mater. Des.* **2018**, *155*, 495–501.
56. Nan, W.; Ghadiri, M. Numerical simulation of powder flow during spreading in additive manufacturing. *Powder Technol.* **2019**, *342*, 801–807. [[CrossRef](#)]
57. Nan, W.; Pasha, M.; Bonakdar, T.; Lopez, A.; Zafar, U.; Nadimi, S.; Ghadiri, M. Jamming during particle spreading in additive manufacturing. *Powder Technol.* **2018**, *338*, 253–262. [[CrossRef](#)]
58. Haferkamp, L.; Liechti, S.; Spierings, A.; Wegener, K. Effect of bimodal powder blends on part density and melt pool fluctuation in laser powder bed fusion. *Prog. Addit. Manuf.* **2021**, *6*, 407–416. [[CrossRef](#)]
59. Haferkamp, L.; Haudenschild, L.; Spierings, A.; Wegener, K.; Riener, K.; Ziegelmeier, S.; Leichtfried, G.J. The Influence of Particle Shape, Powder Flowability, and Powder Layer Density on Part Density in Laser Powder Bed Fusion. *Metals* **2021**, *11*, 418. [[CrossRef](#)]
60. Balbaa, M.A.; Ghasemi, A.; Fereiduni, E.; Elbestawi, M.A.; Jadhav, S.D.; Kruth, J.P. Role of powder particle size on laser powder bed fusion processability of AlSi10Mg alloy. *Addit. Manuf.* **2021**, *37*, 101630. [[CrossRef](#)]
61. Phua, A.; Doblin, C.; Owen, P.; Davies, C.H.; Delaney, G.W. The effect of recoater geometry and speed on granular convection and size segregation in powder bed fusion. *Powder Technol.* **2021**, *394*, 632–644.
62. Xue, K.; Zheng, Y.; Fan, B.; Li, F.; Bai, C. The origin of granular convection in vertically vibrated particle beds: The differential shear flow field. *Eur. Phys. J. E* **2013**, *36*, 8.
63. Chen, H.; Chen, Y.; Liu, Y.; Wei, Q.; Shi, Y.; Yan, W. Packing quality of powder layer during counter-rolling-type powder spreading process in additive manufacturing. *Int. J. Mach. Tools Manuf.* **2020**, *153*, 103553. [[CrossRef](#)]
64. Yao, D.; An, X.; Fu, H.; Zhang, H.; Yang, X.; Zou, Q.; Dong, K. Dynamic investigation on the powder spreading during selective laser melting additive manufacturing. *Addit. Manuf.* **2021**, *37*, 101707. [[CrossRef](#)]

Disclaimer/Publisher's Note: The statements, opinions and data contained in all publications are solely those of the individual author(s) and contributor(s) and not of MDPI and/or the editor(s). MDPI and/or the editor(s) disclaim responsibility for any injury to people or property resulting from any ideas, methods, instructions or products referred to in the content.